TÜBİTAK

Turkish Journal of Earth Sciences

http://journals.tubitak.gov.tr/earth/

Research Article

Turkish J Earth Sci
(2020) 29: 550-578

doi:10.3906/yer-1908-15

APMdisc: An online computer program for the geochemical discrimination of siliciclastic sediments from active and passive margins

María Abdelaly RIVERA-GÓMEZ[1], **John S. ARMSTRONG-ALTRIN**[1,*], **Surendra P. VERMA**[2], **Lorena DÍAZ-GONZÁLEZ**[3]

[1]Unit of Ocean and Coastal Processes, Institute of Marine Sciences and Limnology, National Autonomous University of Mexico, Mexico City, Mexico

[2]Renewable Energy Institute, National Autonomous University of Mexico, Temixco, Morelos, Mexico

[3]Centre for Investigation in Science, Institute of Investigation in Basic and Applied Sciences, Autonomous University of Morelos State, Cuernavaca, Morelos, Mexico

Received: 24.08.2019 • **Accepted/Published Online:** 26.12.2019 • **Final Version:** 16.03.2020

Abstract: An online computer program called APMdisc (**A**ctive and **P**assive **M**argin **disc**rimination) for the discrimination of siliciclastic sediments from active and passive margin settings was written in Java along with the ZK framework. APMdisc calculates four complex discriminant functions ($DF_{ilr(A-P)M}$ and $DF_{mlr(A-P)M}$; $DF_{ilr(A-P)MT}$ and $DF_{mlr(A-P)MT}$), which represent linear combinations of log-ratios of all ten major elements (M) and ten major and six trace elements (MT), respectively. In these equations, ilr and mlr stand for isometric log-ratio and modified log-ratio transformations of the chemical composition of active and passive margin sediments, respectively. The ilr transformation provided the same results as the mlr as documented for five case studies of Quaternary sediments from California, Antarctica, Nigeria, India, and Japan. We also present 9 other case studies (for Neogene to Quaternary sediments from known tectonic settings) and 11 application studies (Tertiary to Neoproterozoic sediments and sedimentary rocks) to show the functioning of the multidimensional discrimination proposed in this paper. In most cases, the results from the APMdisc were consistent with the literature conclusions inferred from different geological and geochemical techniques. Nevertheless, APMdisc provides probability estimates for both tectonic settings, which allows the decision to be made based on the probability concept. We also added a new Robustness module to APMdisc, which allows the user to test the robustness of a sample against field changes, such as weathering and diagenesis, and laboratory analytical errors or uncertainties. This program can therefore be recommended for deciphering the margin type of older terrains. The APMdisc program can be used online by researchers for tectonic discrimination based on sediment composition. The users can process the data file at our web portal http://tlaloc.ier.unam.mx.

Key words: Data processing, sedimentology, geostatistics, tectonic discrimination, multidimensional techniques

1. Introduction

The tectonic discrimination of sediments from active and passive margins has been of much interest (e.g., Dickinson and Suczek, 1979; Kirkwood et al., 2016). In order to infer the tectonic setting of an unknown basin, researchers are traditionally using the old tectonic discrimination diagrams proposed by Bhatia (1983), Bhatia and Crook (1986), and Roser and Korsch (1986), even though Armstrong-Altrin and Verma (2005), Verma and Armstrong-Altrin (2013, 2016), Basu et al. (2016), and Verma (2020), among others, have cautioned about the low efficiency of these old diagrams to discriminate tectonic environments.

Recently, new multidimensional tectonic discriminant function diagrams have been proposed, not only for clastic sediments (Verma and Armstrong-Altrin, 2013, 2016) but also for a variety of igneous rocks (e.g., see Verma, 2020 for more details). The new diagrams and functions for clastic sediments were based on a worldwide database of major and trace element concentrations of Quaternary to Miocene sediments, compiled from various sources. Later, Verma et al. (2016a) created the software "TecSand" to discriminate three tectonic settings (arc, rift, and collision) for the multidimensional diagrams proposed by Verma and Armstrong-Altrin (2013). The TecSand software has been successfully used, and its high efficiency to discriminate tectonic environments was addressed by various researchers from different parts of the world (e.g., Tapia-Fernandez et al., 2017; Papadopoulos, 2018; Prakash et al., 2018; Ramos-Vázquez et al., 2018; Tawfik et al., 2018; Zaid et al., 2018; Ngueutchoua et al., 2019). However, a

* Correspondence: armstrong@cmarl.unam.mx

computer program for the discriminant functions of Verma and Armstrong-Altrin (2016) to discriminate active and passive margin settings has not been proposed yet, which could facilitate the use of complex discriminant functions and evaluate the robustness of the multidimensional approach.

In order to fill this gap, using both isometric log-ratio (ilr; Egozcue et al., 2003) and modified log-ratio (mlr, also called hybrid log-ratio hlr; Verma, 2020; more details are provided in Appendix I) transformations, we created a new program, APMdisc, to discriminate clastic sediments from active and passive margin settings. To construct APMdisc, we have programmed four new complex functions using both ilr and mlr, as explained in the following section. Similarly, to quantify the functioning of the APMdisc program, we present 14 test studies and 11 application studies to discriminate sediments from active and passive margin settings. For all test case studies, the diagrams indicated the expected tectonic setting, whereas for application studies, the APMdisc program indicated an active or passive margin with generally high percent success values.

2. Methodology

2.1. Multidimensional functions using ilr and mlr transformations for the geochemical discrimination of siliciclastic sediments from active and passive margin settings

The database used for proposing new major element-based discriminant functions consisted of complete data of 10 major elements (M; SiO_2 to P_2O_5) for 3246 samples; among them, 1760 samples represent an active (A) margin and 1486 represent a passive (P) margin. Similarly, for functions based on combined major and trace elements (MT; SiO_2 to P_2O_5, Cr, Nb, Ni, V, Y, and Zr), the database included 361 and 448 samples from active and passive margins, respectively. We limited our proposal to only these 6 trace elements for multiple reasons: (1) these trace elements, along with all major elements, can be routinely determined by one of the most commonly used analytical techniques of X-ray fluorescence spectrometry (e.g., Rollinson, 1993; Verma, 2020); (2) increasing the number of trace elements by incorporating other useful elements, such as Co, Hf, Sc, Ta, or the rare-earth elements (e.g., Cullers, 2002), drastically decreased the number of samples for training the discriminant functions, to the extent that we did not consider them as representative of the entire earth; (3) the use of additional elements, generally requiring more powerful and costly analytical techniques, such as inductively coupled plasma mass spectrometry or neutron activation analysis, not widely available in most developing countries, would have reduced the application of the discriminant functions by users who do not have access to such techniques; and (4) the 6 elements used, in addition to the 10 major elements, showed adequate statistical differences between the two groups (active and passive margins) and high discriminating power as documented later in this section. The use of additional elements having high discriminating power should, therefore, await the availability of additional reports with comprehensive geochemical analysis for updating the database and making it representative of the problem at hand.

The sample types included are clastic sediments and rocks (clay, mud, silt, claystone, mudstone, siltstone, sand, and sandstone) from different parts of the world, compiled from various literature sources (Figure 1). More details about sample locations and sources were provided by Verma and Armstrong-Altrin (2016).

The major element (M) data were first adjusted to 100% on an anhydrous basis as indicated in Table AI-1 (Appendix I). The ilr ($ilr1_{TiM}$ to $ilr9_{PM}$) and mlr ($mlr1_{TiM}$ to $mlr9_{PM}$) values for the major elements are given in Tables AI-2 and AI-3, respectively ($_{Ti} = TiO_2$ and $_{P} = P_2O_5$). Similarly, all 16 major and trace elements (MT) were also adjusted to 100% (Table AI-4) and the transformed values were calculated ($ilr1_{TiMT}$ to $ilr15_{ZrMT}$; Table AI-5; and $mlr1_{TiMT}$ to $mlr15_{ZrMT}$; Table AI-6) (MT = major and trace elements).

The computer program DOMuDaF (Verma et al., 2016b) was then used to obtain multinormally distributed samples in the ilr and mlr spaces separately for the two groups (active and passive margins). These multivariate data were tested to examine the statistical similarities and differences between the two groups from Wilks lambda and F tests (Tables AI-7 and AI-8). For major elements, all variables, except Mg, showed very low P-values, implying that all, except probably Mg, have high discriminating power (Ca showing the highest F value; Table AI-7). For combined major and trace elements also, 11 variables showed high discriminating power (Nb showing the highest F value; Table AI-8), with the remaining 4 elements (Fe, K, Cr, and V) showing less differences between the two groups. Nevertheless, all elements can be used for multidimensional discrimination.

The multinormally distributed ilr and mlr transformed variables were used for linear discriminant and canonical analysis for the discrimination of active and passive margins. The "Discriminant Analysis" submodule in the "Multivariate Exploratory Techniques" module of Statistica was used under the probability option "Same for all groups" and provided the so-called "Raw coefficients". These "Raw coefficients" were used to construct four discriminant functions, $DF_{ilr(A-P)M}$ and $DF_{ilr(A-P)MT}$ (Tables AI7 and AI8) and $DF_{mlr(A-P)M}$ and $DF_{mlr(A-P)MT}$ for the subdivision of active

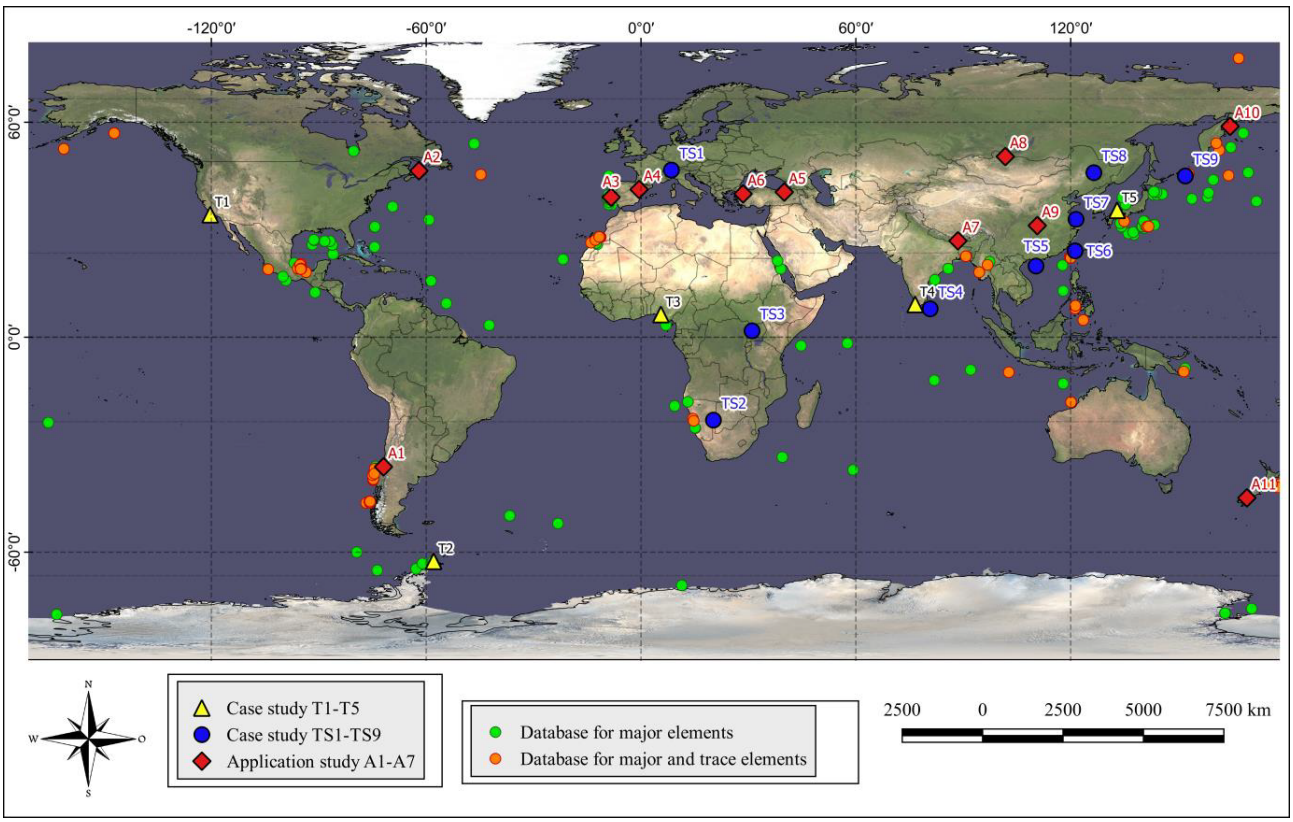

Figure 1. Schematic location of sampling sites for cases studies T1–T5 from Verma and Armstrong-Altrin (2016), 4 case studies TS1–TS4 used earlier by Verma and Armstrong-Altrin (2016), and 5 new cases studies TS5–TS9 and 11 application studies A1–A11; symbols are explained in inset. The locations used for proposing the discriminant functions are also shown; more details on the training set samples are given by Verma and Armstrong-Altrin (2016).

and passive for "M" and "MT" in the multidimensional ilr and mlr spaces, respectively.

The multidimensional discrimination diagrams for the active and passive margins are available in Appendix II (Figures AII-1 and AII-2). The centroids are $C_{ilr,mlr(A)M}$ = 0.8470 and $C_{ilr,mlr(P)M}$ = –1.0032, and the discrimination boundary is $_{ilr,mlr}(A\text{-}P)_{boundaryM}$ = –0.0784, for the scheme based on major elements. The centroids are $C_{ilr,mlr(A)MT}$ = –1.3744 and $C_{ilr,mlr(P)MT}$ = 1.1075, and the discrimination boundary is $_{ilr,mlr}(A\text{-}P)_{boundaryMT}$ = –0.13345, for the scheme based on combined major and trace elements.

The percent success values obtained for the discrimination system based on major element are 87.2% and 83.8% for active and passive margins, respectively (Figure AII-1). The percent success is defined here as the ratio of the number of correctly discriminated samples to the total number of samples, expressed in percent. Similarly, for the discrimination system based on combined major and trace elements, these values are 97.0% and 85.7% for the active and passive margins, respectively (Figure AII-2). These percent success values are similar to those reported by Verma and Armstrong-Altrin (2016). We also note that the percent success is higher for higher dimensions (10 versus 16; major elements versus combined major and trace elements), which is consistent with other studies of multidimensional solutions (e.g., Verma, 2020; Verma and Díaz-González, 2020). Also, note that the group centroids are farther apart in the MT in comparison with the M diagram, which means that the MT diagram is likely to provide higher success than the M diagram (Verma, 2020).

The centroids, the boundaries, and the percent success obtained through the ilr transformation were the same as those of the mlr transformation, implying that both transformations should provide the same results.

2.2. Computer program

The online computer program APMdisc (**A**ctive and **P**assive **M**argin **disc**rimination) was written in Java along with the ZK framework to efficiently discriminate the clastic sediments from active and passive margin settings (Figure 2). First, the user must prepare an Excel file from the template provided for inputting data on the web portal tlaloc.ier.unam.mx. It is important that Fe be input as total $Fe_2O_3^t$ (and not as FeO^t, nor as the two-oxidation varieties; the first equation in Table AI-1 for Fe-conversion must be

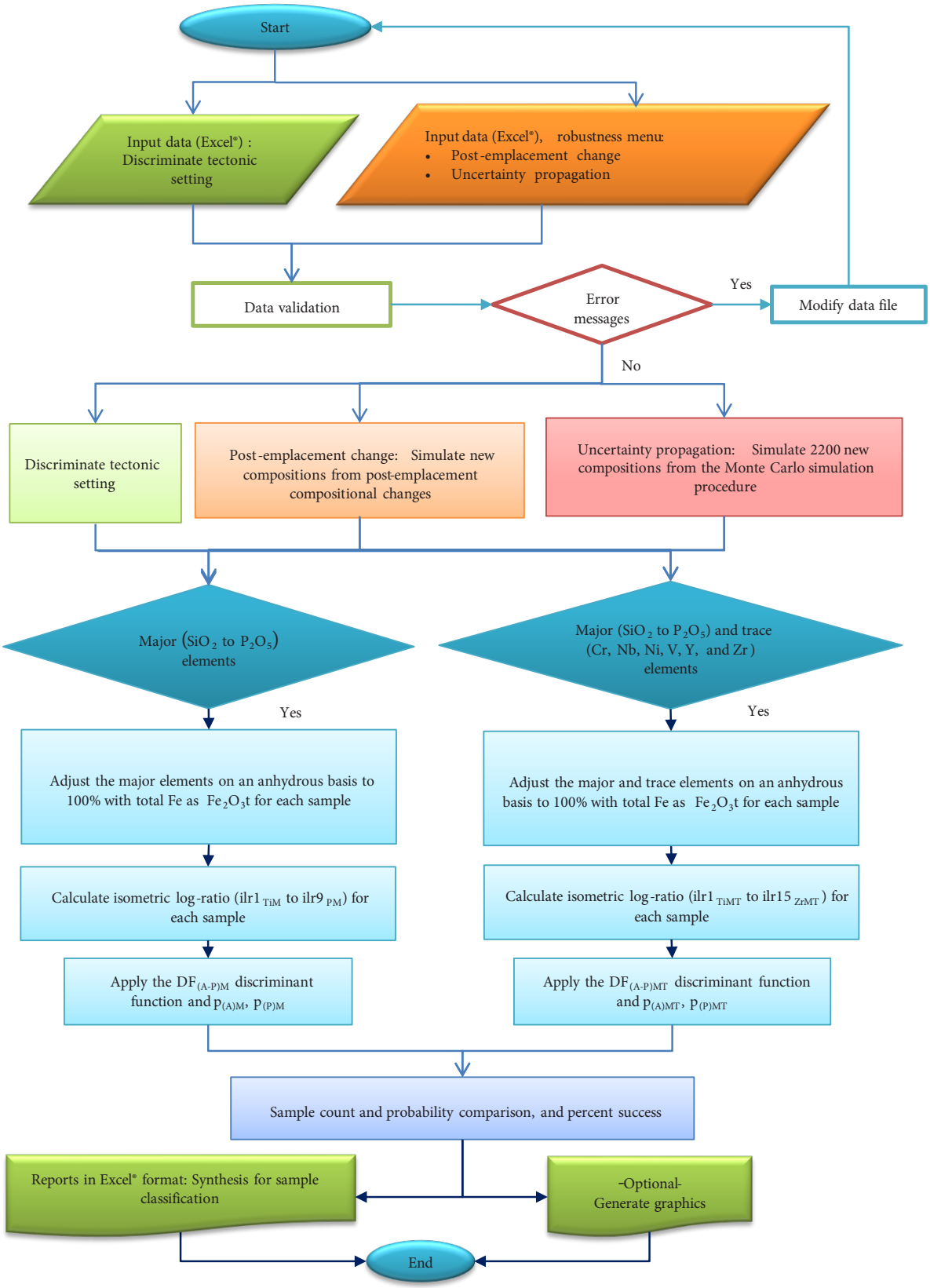

Figure 2. Schematic flow diagram of the new computer program, APMdisc, including its Robustness module. The abbreviations used are as follows: ilr–isometric log-ratio transformation; A–Active; P–Passive; M–major element; T–trace element; p–probability.

used and Fe properly input as $Fe_2O_3^t$ before accessing the program). After opening the program, the user must open the data file in the program APMdisc to process the data. If the input file is error-free, the program will indicate that the user can proceed to process the data. Otherwise, the user will have to edit the data file in Excel and make it error-free. The program under use will then adjust the major (Table AI-1) and combined major and trace elements (Table AI-4) data to 100% on an anhydrous basis and then proceed for further calculations.

APMdisc will convert the variables to ilr (Tables AI-2 and AI-5) or mlr (Tables AI-3 and AI-6) transformation, apply the discriminant functions and perform the respective probability calculations to assign each sample to an active or a passive margin. The program gives an output of mean probability and respective standard deviation values, as well as the sample count as percent success, which represents the percentage of the number of samples (out of the total number under study) that plotted correctly in the mentioned field (active or passive). The program also counts the samples in terms of their probabilities for the respective fields and provides a synthesis based on the probability counts. Such counts are useful in the case of controversy, such as when an equal number of samples plot in both fields (see Figures AII-1 and AII-2 for the boundaries of the two fields).

The APMdisc provides two data files, the first with all the calculations and results for each sample (extended report), and the second a brief report or resume of results. Furthermore, the user can visualize and download the diagrams in JPEG format.

Following Verma and Díaz-González (2020), as a further improvement of the APMdisc program, we have incorporated a Robustness module to better understand the effects of field changes (such as weathering, transportation, deposition, and diagenesis; e.g., Basu et al., 2016) and laboratory analysis uncertainties (Verma et al., 2018, 2019; Verma, 2020). This module is added to the original version of the APMdisc (Figure 2). Two separate templates are available for use by anyone to test his or her own data for robustness against percent gain or loss of one or more elements as well as against analytical errors or uncertainties.

For easy online use of our proposed scheme, we have made APMdisc available to all potential users through our web portal http://tlaloc.ier.unam.mx/apmdisc. Anyone can easily access this online program and use our software after registration and log-in. Nevertheless, the complete information is also presented in this work for those who wish to construct their own tool.

2.3. Performance of log ratio transformations

To illustrate the comparison of the performance of the two transformations (ilr and mlr) for the multidimensional discrimination of active and passive margins, we selected five case studies, T1–T5, from California, Antarctica, Nigeria, India, and Japan, used by Verma and Armstrong-Altrin (2016) (Table 1; Figure 1 for schematic locations of T1-T5). The modified log-ratio transformation (mlr; used by Verma and Armstrong-Altrin, 2016; see Tables AI-3 and AI-6) is different from the other transformations (additive log-ratio alr and centered log-ratio clr, proposed by Aitchison, 1986; and isometric log-ratio ilr proposed by Egozcue et al., 2003). The results showed that the mathematical properties of the log-ratio transformations (ilr and mlr) are no longer important if the multidimensional technique involves LDA (Figures AII-3a-e and AII-4a-e), which is consistent with Verma (2015, 2020) who showed that all four transformations (alr, clr, ilr, and mlr or hlr) provide exactly the same results when LDA is applied to any given database. The results and the discussion of the case studies T1-T5 are available for download at http://tlaloc.ier.unam.mx/apmdisc.

3. Results

The correct functioning of the APMdisc program is tested by the test (TS1–TS9) and application (A1–A11) studies. The results obtained by the statistical analysis are described in this section and listed in Tables 2 and 3, and are further illustrated in Figures 3a–3i, 4a–4h, 5a–5l, and 6a–6k.

3.1. Case studies of Quaternary sediments from known tectonic setting

We present 9 test case studies, TS1–TS9, of Quaternary sediments from known tectonic settings to test the correct functioning of discriminant functions proposed in this work (Table 2; Figures 2, 3a–3j, and 4a–4i). The geochemical database used for these case studies is different from the database utilized for proposing the two discriminant functions (Figures AII-1 and AII-2). The discriminant functions for the diagrams based on major elements (Table AI-9) and combined major and trace elements (Table AI-10) were calculated from the new online computer program APMdisc. Since the ilr and mlr transformations provided the same results (Case Studies T1–T5; Section 2.3), we decided to apply only the ilr transformation (Egozcue et al., 2003) for all other case studies.

3.1.1. Case study TS1 (Central Alps, Switzerland)

Von Eynatten et al. (2012) reported geochemical data for young (<300 years old) clastic sediments from modern glaciers of the Central Alps, Switzerland. Out of 161 samples with complete major element data, 129 plotted in the active margin field in Figure 3a, with mean probability value of 0.846, signifying 80.1% success in terms of sample counts (Table 2). The combined major and trace element data were available for 102 samples. Out of these 102 samples, 91 plotted in the active margin field in Figure 4a

Table 1. Results obtained for case studies (T1–T5),* which are tested for confirming the similarity between ilr and mlr log transformations**.

Case study	Figure type (no. of samples)	Statistics n (mean ± standard deviation probability)		Percent success (%)	Authors' inferred tectonic setting	Verma and Armstrong-Altrin (2016)	Reference
		Active margin (A)	Passive margin (P)				
T1	M (267)	0 (0)	267 (0.918 ± 0.027)	100% (P)	Not discussed	Passive	Tada et al. (2000)
	MT (99)	1 (0.523)	98 (0.784 ± 0.095)	99% (P)			
T2	M (30)	28 (0.799 ± 0.113)	2 (0.784 ± 0.214)	93% (A)	Island arc	Active	Lee et al. (2004)
	MT (26)	25 (0.998 ± 0.003)	1 (0.972)	96% (A)			
T3	M (18)	0 (0)	18 (0.926 ± 0.114)	100% (P)	Rift	Passive	Imasuen et al. (1989)
	MT (18)	0 (0)	18 (0.975 ± 0.102)	100% (P)			
T4	M (35)	8 (0.623 ± 0.068)	27 (0.805 ± 0.160)	77% (P)	Not discussed	Passive	Paul (2001)
	MT (35)	0 (0)	35 (0.989 ± 0.038)	100% (P)			
T5	M (49)	46 (0.791 ± 0.127)	3 (0.661 ± 0.132)	94% (A)	Arc	Active	Ishiga et al. (2000)
	MT (49)	49 (0.961 ± 0.049)	0 (0)	100% (A)			

* Verma and Armstrong-Altrin (2016); ** The results obtained from both ilr (isometric log-ratio) and mlr (modified log-ratio) transformations are available in the APMdisc program (http://tlaloc.ier.unam.mx). All are siliciclastic sediments of Quaternary period. M = Major element; MT = major and trace elements. T1: Santa Barbara Basin, southern California; T2: King George Island, West Antarctica; T3: Benin City, Nigeria; T4: Kerala, India; T5: Lake Shinji, Japan.

Table 2. Case studies for testing the APMdisc program by Quaternary siliciclastic sediments (Miocene to Holocene age).

Case study	Figure type (no. of samples)	Figure number	Statistics n (mean ± standard deviation probability)		Percent success (%)	Authors' inferred tectonic setting	Reference
			Active margin (A)	Passive margin (P)			
TS1	M (161)	Figure 3a	129 (0.846 ± 0.141)	32 (0.690 ± 0.125)	80.1% (A)	Not discussed	von Eynatten et al. (2012)
	MT (102)	Figure 4a	91 (0.831 ± 0.119)	11 (0.705 ± 0.109)	89.2% (A)		
TS2	M (16)	Figure 3b	0 (0)	16 (0.909 ± 0.075)	100% (P)	Not discussed	Vermeesch and Garzanti (2015)
	MT (16)	Figure 4b	2 (0.605 ± 0.043)	14 (0.860 ± 0.145)	88% (P)		
TS3	M (60)	Figure 3c	6 (0.723 ± 0.137)	54 (0.902 ± 0.112)	90% (P)	Rifted margin	Schneider et al. (2016)
	MT (60)	Figure 4c	3 (0.702 ± 0.138)	57 (0.984 ± 0.066)	95% (P)		
TS4	M (47)	Figure 3d	3 (0.759 ± 0.081)	44 (0.936 ± 0.093)	94% (P)	Not discussed	Young et al. (2014)
	MT (46)	Figure 4d	10 (0.769 ± 0.155)	36 (0.854 ± 0.147)	78% (P)		
TS5	M (26)	Figure 3e	0 (0)	26 (0.957 ± 0.105)	100% (P)	Passive	Pe-Piper et al. (2016)
	MT (20)	Figure 4e	0 (0)	20 (1.0 ± 0.0)	100% (P)		
TS6	M (23)	Figure 3f	4 (0.868 ± 0.137)	19 (0.777 ± 0.109)	83% (P)	Passive	Garzanti and Resentini (2016)
	MT (23)	Figure 4f	3 (0.874 ± 0.177)	20 (0.938 ± 0.083)	87% (P)		
TS7	M (62)	Figure 3g	0 (0)	62 (0.892 ± 0.052)	100% (P)	Ridge	Rao et al. (2015)
	MT (62)	Figure 4g	2 (0.532 ± 0.027)	60 (0.857 ± 0.113)	97% (P)		
TS8	M (14)	Figure 3h	0 (0)	14 (0.840 ± 0.060)	100% (P)	Not discussed	Xie and Chi (2016)
	MT (14)	Figure 4h	1 (0.663)	13 (0.854 ± 0.143)	93% (P)		
TS9	M (12)	Figure 3i	12 (0.993 ± 0.008)	0 (0)	100% (A)	Arc	Sattarova and Artemova (2015)
	MT (0)	---	(--)	(--)	(--)		

M = Major element; MT = major and trace elements. TS1: Switzerland; TS2: Namibia; TS3: Uganda; TS4: Sri Lanka; TS5: Hainan island, China; TS6: Taiwan River, Japan; TS7: Yellow Sea, China; TS8: Harbin, China; TS9: Kuril-Kamchatka.

Table 3. Application studies for testing the APMdisc program by Precambrian to Cretaceous siliciclastic sediments and rocks.

Application study	Age	Figure type (no. of samples)	Figure number	Statistics n (mean ± standard deviation probability) of the samples discriminated as		Percent success (%)	Authors' inferred tectonic setting	Reference
				Active margin (A)	Passive margin (P)			
A1	Ordovician	M (8)	Figure 5a	0 (0)	8 (0.955 ± 0.046)	100% (P)	Extensional tectonics	Abre et al. (2011)
		MT (8)	Figure 6a	1 (0.510)	7 (0.953 ± 0.094)	88% (P)		
A2	Cretaceous-Jurassic	M (361)	Figure 5b	27 (0.766 ± 0.153)	334 (0.905 ± 0.115)	93% (P)	Passive	Zhang et al. (2014)
		MT (356)	Figure 6b	18 (0.645 ± 0.122)	338 (0.966 ± 0.085)	95% (P)		
A3	Carboniferous	M (74)	Figure 5c	57 (0.838 ± 0.151)	17 (0.785 ± 0.134)	77% (A)	Active margin	Jorge et al. (2013)
		MT (74)	Figure 6c	67 (0.973 ± 0.063)	7 (0.801 ± 0.161)	91% (A)		
A4	Albian	M (40)	Figure 5d	1 (0.992)	39 (0.885 ± 0.109)	98% (P)	Rift	López et al. (2005a, b)
		MT (40)	Figure 6d	4 (0.766 ± 0.207)	36 (0.922 ± 0.095)	90% (P)		
A5a	Lower Jurassic	M (15)	Figure 5e	13 (0.919 ± 0.11)	2 (0.992 ± 0.006)	87% (A)	No inference	Dokuz and Tanyolu (2006)
		MT (9)	Figure 6e	7 (0.936 ± 0.133)	2 (0.775 ± 0.204)	78% (A)		
A5b	Upper Cretaceous	M (21)	Figure 5f	18 (0.916 ± 0.118)	3 (0.667 ± 0.12)	86% (A)		
		MT (10)	Figure 6f	7 (0.912 ± 0.126)	3 (0.836 ± 0.209)	70% (A)		
A6	Jurassic	M (23)	Figure 5g	10 (0.839 ± 0.142)	13 (0.830 ± 0.136)	56% (P)	Passive	Sengün and Koralay (2019)
		MT (0)	---	---	---	---		
A7	Tertiary	M (16)	Figure 5h	10 (0.785 ± 0.09)	6 (0.692 ± 0.132)	62% (A)	Passive	Kundu et al. (2016)
		MT (16)	Figure 6g	15 (0.813 ± 0.154)	1 (0.748 ± 0.0)	94% (A)		
A8	Cambrian-Ordovician	M (15)	Figure 5i	15 (0.913 ± 0.069)	0 (0)	100% (A)	Arc	Chen et al. (2014)
		MT (13)	Figure 6h	9 (0.965 ± 0.065)	4 (0.975 ± 0.026)	69% (A)		
A9	Neoproterozoic	M (27)	Figure 5j	27 (0.959 ± 0.091	0 (0)	100% (A)	Arc	Xiang et al. (2015)
		MT (27)	Figure 6i	27 (1.000 ± 0.001)	0 (0)	100% (A)		
A10	Middle Eocene to Early Miocene	M (25)	Figure 5k	25 (0.887 ± 0.077)	0 (0)	100% (A)	Active	Ledneva et al. (2004)
		MT (25)	Figure 6j	25 (0.966 ± 0.037)	0 (0)	100% (A)		
A11	Triassic	M (24)	Figure 5l	24 (0.892 ± 0.129)	0 (0)	100% (A)	Arc	Coombs et al. (2000)
		MT (24)	Figure 6k	24 (0.996 ± 0.006)	0 (0)	100% (A)		

A1: Ponón Trehué and Pavón Formations, Argentina; A2: Scotian Basin, Canada; A3: Baixo Alentejo Flysch Group, Portugal; A4: Oliete Basin, Spain;
A5: eastern Pontides, NE Turkey; A6: Sakarya Zone, NW Turkey; A7: Middle Siwalik, Himalayas; A8: Altai-Mongolian Terrane, Russia-Mongolia; A9: Yangtze Block, China; A10: Karaginski Island, Kamchatka; A11: Beach-Brighton, New Zealand.

and showed mean probability of 0.831 and percent success of 89.2% in terms of sample counts (Table 2). Thus, both diagrams (Figures 3a and 4a) provided a consistent result of an active margin for the Central Alps in Switzerland (Table 2). This result is compatible with the general geology of the Swiss Alps.

3.1.2. Case study TS2 (Namibia)

Vermeesch and Garzanti (2015) reported major and trace element data of 16 Quaternary sediment samples from Namibia. These samples indicated a passive margin setting in Figures 3b and 4b, with mean probability values of 0.909 and 0.860, respectively (Table 2). This result is consistent with the general geology of Namibia as well as with the conclusions derived by the original authors.

3.1.3. Case study TS3 (Uganda)

Schneider et al. (2016) reported major and trace element data for 60 Quaternary sediment samples from the Albertine rift, Uganda. Most samples indicated a passive margin setting in both diagrams, one based on major elements and the other on major and trace elements, with percent success between 90% and 95%, respectively (Figures 3c and 4c; Table 2). This interpretation is consistent with the

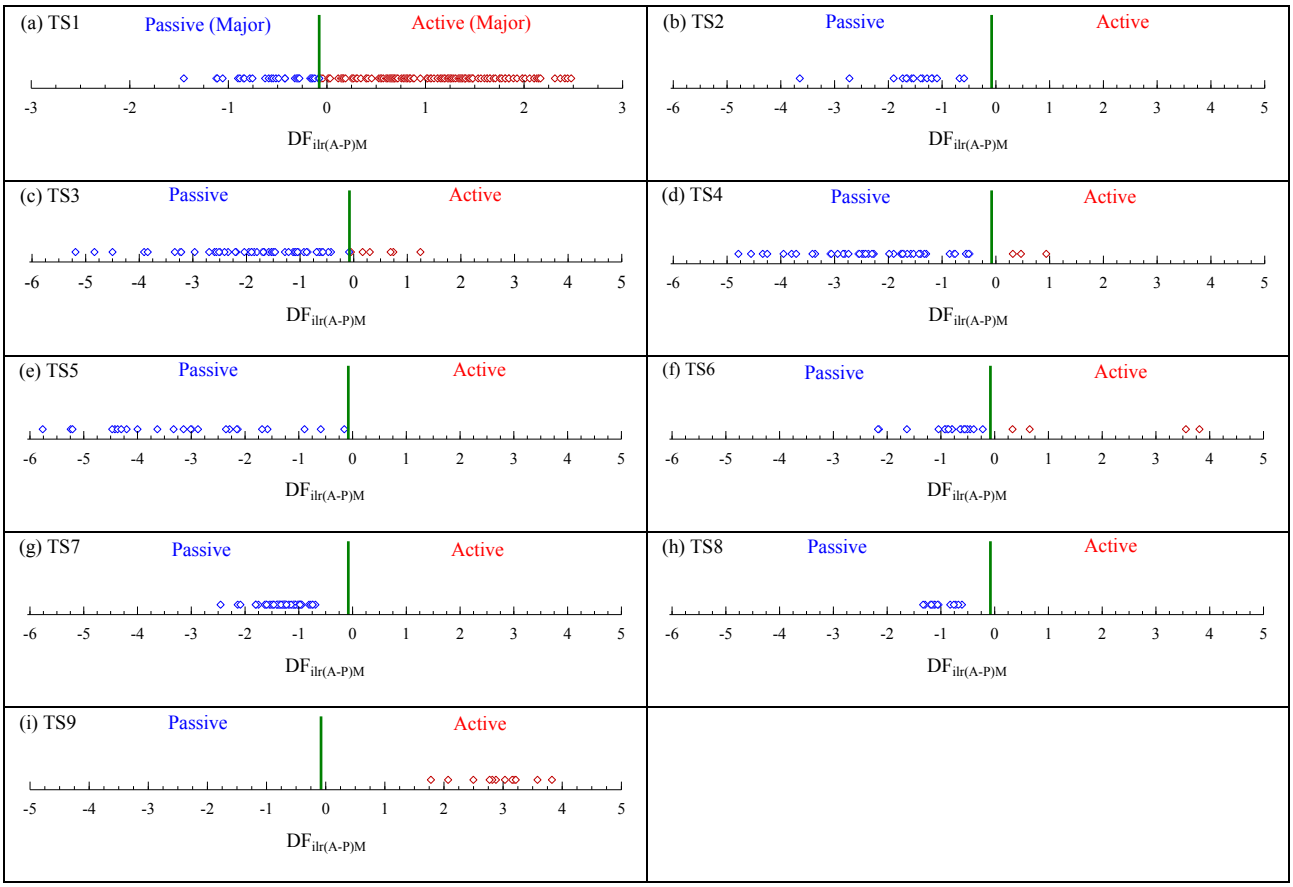

Figure 3. One-axis discriminant function $DF_{ilr(A-P)M}$ diagram for the subdivision of Active (A) and Passive (P) margins (Table AI-11) based on isometric (i) log-ratio transformation of major elements (M), shows test studies TS1–TS9 (Table 2), where a) TS1: Eynatten et al. (2012); b) TS2: Vermeesch and Garzanti (2015); c) TS3: Schneider et al. (2016); d) TS4: Young et al. (2014); e) TS5: Pe-Piper et al. (2016); f) TS6: Garzanti and Resentini (2016); g) TS7: Rao et al. (2015); h) TS8: Xie and Chi (2016); i) TS9: Sattarova and Artemova (2015).

original authors (Schneider et al., 2016); they proposed a rift setting for the Uganda river sediments.

3.1.4. Case study TS4 (Sri Lanka)

In this case study, we compiled geochemical data for 47 Quaternary sediment samples from the Trincomalee Bay, Sri Lanka, which were reported by Young et al. (2014). Out of 47 samples, 44 plotted in the passive margin field of the major element-based diagram with high mean probability (0.936) (Figure 3d; Table 2). Similarly, 36 samples (out of 46) plotted in the passive margin field of the major and trace element-based diagram (Figure 4d; Table 2). Although the original authors did not discuss the tectonic setting of the study area, the passive margin setting derived from these diagrams is consistent with the geology of the Trincomalee Bay (Figure 1).

3.1.5. Case study TS5 (Hainan Island)

Geochemical data of 26 Quaternary sediments from the river and delta, Hainan Island, China, were compiled (Pe-Piper et al., 2016). For the major element-based discriminant function (Table AI-9), 26 samples had complete data (Table 2) and all samples were plotted in the passive margin field with high mean probability (0.957) (Figure 3e). Out of these 26 samples, only 20 had complete data for the second discriminant function based on the combination of major and trace elements (Table AI-10; mean probability of 1.000 in Table 2). On this plot, all 20 samples (100%) were plotted in the passive margin field (Figure 4e), suggesting a passive margin setting for the sediments derived from Hainan Island.

3.1.6. Case study TS6 (Taiwan River)

Geochemical data of Quaternary sands from the Taiwan River were compiled from Garzanti and Resentini (2016). Twenty-three samples were available for the discriminant function based on major elements (Table 2). In Figure 3f, among 23 samples, 19 samples plotted in the passive margin field with an average probability value of 0.777 (about 83% success for passive margin; Table 2). Similarly, based on the combination of major and trace elements,

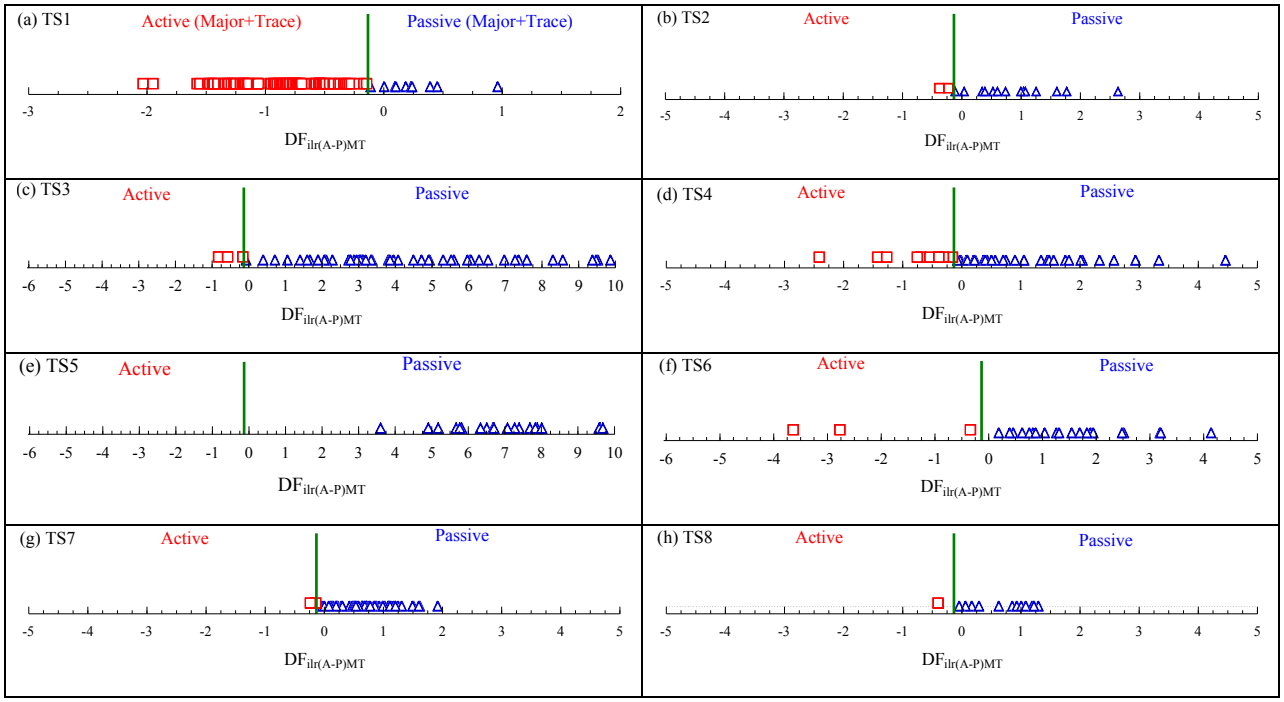

Figure 4. One-axis discriminant function $DF_{ilr(A-P)MT}$ diagram for the subdivision of Active (A) and Passive (P) margins (Table AI-12) based on isometric (i) log-ratio transformation of system based on combined major and trace elements (MT), shows test studies TS1–TS9 (Table 2), where a) TS1: Eynatten et al. (2012); b) TS2: Vermeesch and Garzanti (2015); c) TS3: Schneider et al. (2016); d) TS4: Young et al. (2014); e) TS5: Pe-Piper et al. (2016); f) TS6: Garzanti and Resentini (2016); g) TS7: Rao et al. (2015); h) TS8: Xie and Chi (2016).

most of the samples showed a passive margin field (n = 20) with a mean probability of 0.938 (Figure 4f; about 87% success for P in Table 2). This interpretation is consistent with the results reported by the original authors.

3.1.7. Case study TS7 (Yellow Sea, China)

Geochemical data of 62 Quaternary surface sediments from the Yellow Sea, China (Rao et al., 2015), indicated a passive margin setting for the discriminant functions, one based on major elements (all 62 samples; Figure 3g) and the other of major and trace element concentrations (all 62 samples; Figure 4g). The respective percent success values for the passive margin (P) were 100% and 97%, respectively, for M (Table AI-9) and MT (Table AI-10) functions (Table 2). Thus, these diagrams revealed a passive margin for the Yellow Sea sediments.

3.1.8. Case study TS8 (Harbin, China)

The geochemical data of 14 Quaternary sediment samples from Harbin, China, was compiled from Xie and Chi (2016). In the major element-based diagram, all samples plotted in the passive margin field with mean probability value of 0.840 (Figure 3h). On the other hand, in the major and trace element-based diagram, 13 plotted in the passive margin field with mean probability of 0.854 (Figure 4h; Table 2).

3.1.9. Case study TS9 (Kuril-Kamchatka)

Sattarova and Artemova (2015) reported 12 deep-sea sediment samples recovered from the Kamchatka trench; all the samples were plotted in the active margin field of the major element-based diagram (Figure 3i; mean probability of 0.993 in Table 2). This interpretation is also consistent with the original authors. The authors did not report Nb, Y, and Zr data; therefore, the major and trace element-based diagram was not tested.

3.2. Application studies from older rocks

We present 11 application studies (A1-A11 in Table 3; Figures 5a–5l and 6a–6k) to highlight the use of our discriminant function diagrams for older terrains.

3.2.1. Application study A1 (Argentina)

Our first application study is from Abre et al. (2011), who reported geochemical data for 8 Ordovician sandstone and mudstone samples from Argentina. All 8 samples plotted within the passive margin field in the major element-based diagram (Figure 5a). Similarly, 7 samples plotted in the passive margin field of the major and trace element-based diagram (Figure 6a). Therefore, a passive margin setting could be inferred for the Ordovician samples compiled from Abre et al. (2011), with mean probability values of 0.955 and 0.953, respectively, for M and MT diagrams

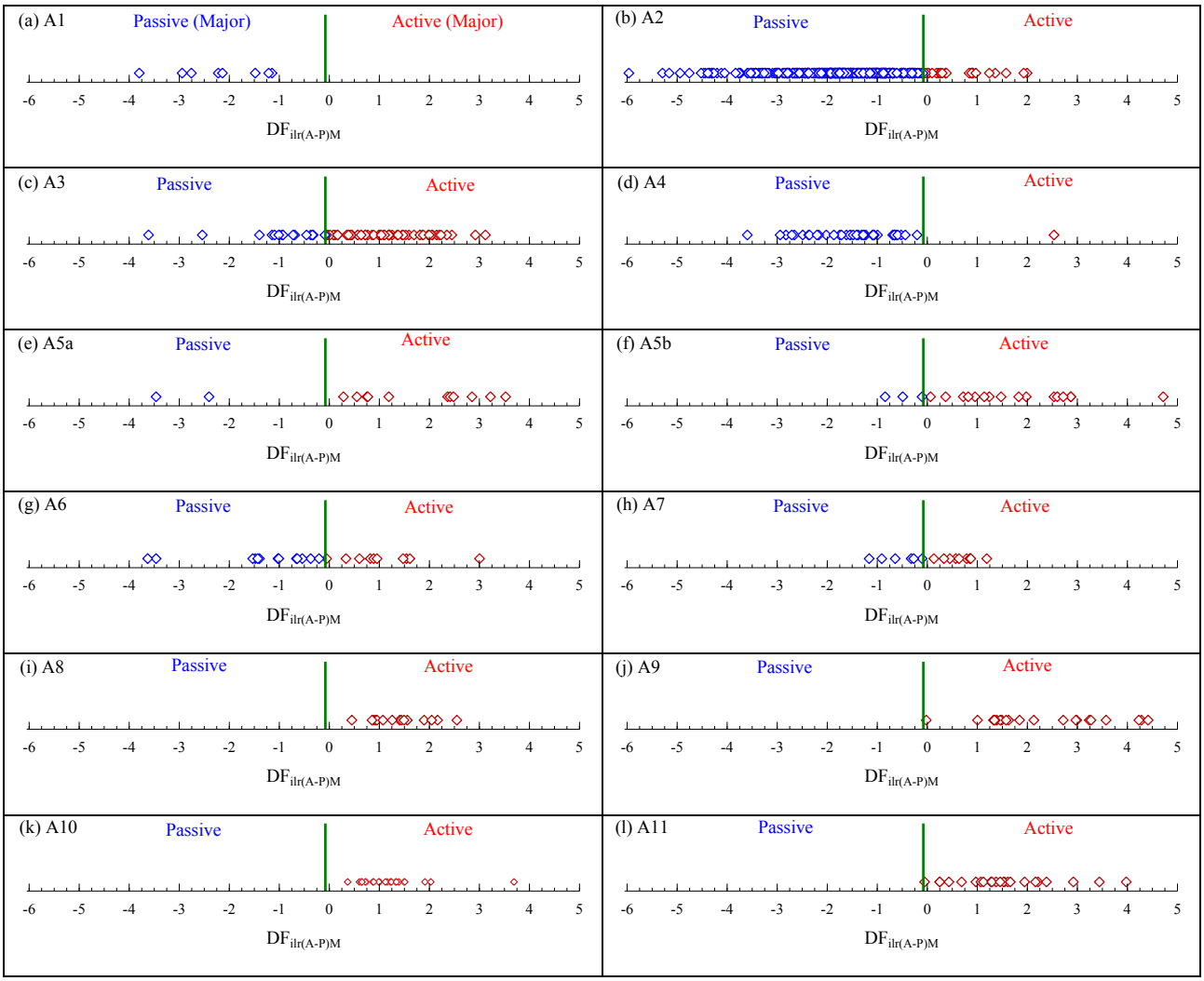

Figure 5. One-axis discriminant function $DF_{ilr(A-P)M}$ diagram for the subdivision of Active (A) and Passive (P) margin (Table AI-11) based on isometric (i) log-ratio transformation of major elements (M), shows applications A1–A11 (Table 3), where a) A1: Abre et al. (2011); b) A2: Zhang et al. (2014); c) A3: Jorge et al. (2013); d) A4: Lopez et al. (2005a, b); e) A5a: Dokuz and Tanyolu (2006); f) A5b: Dokuz and Tanyolu (2006); g) A6: Sengün and Koralay (2019); h) A7: Kundu et al. (2016); i) A8: Chen et al. (2014); j) A9: Xiang et al. (2015); k) A10: Ledneva et al. (2004); l) A11: Coombs et al. (2000).

(Table 3). The original authors (Abre et al., 2011) proposed an extensional tectonic setting for their study area, which was based on geological considerations. Our inference of a passive margin is consistent with their proposal.

3.2.2. Application study A2 (Canada)

Zhang et al. (2014) reported geochemical data for the Cretaceous-Jurassic sandstone and mudstone samples from the Scotian Basin, Canada (361 data for major and 356 for major and trace elements). In the major element-based diagram, most of the samples plotted in the passive margin field (334 out of 361) with a high mean probability value of 0.905 (Figure 5b; about 93% percent success for P in Table 3). Similarly, in Figure 6b, 338 out of 356 samples plotted in the passive margin field with a very high mean probability value of 0.966 (about 95% percent success for P in Table 3). Therefore, a passive margin setting is indicated for the Scotian Basin. This interpretation is consistent with the original authors (Zhang et al., 2014), because they mentioned that the Scotia Basin was a Mesozoic-Cenozoic passive margin basin on the Atlantic margin of southeastern Canada. Similarly, based on the detrital mineral modal compositions, they interpreted that the studied sediments were derived from the Labrador rift.

3.2.3. Application study A3 (Portugal)

The geochemical data for 74 samples of Carboniferous shale and greywacke from the Baixo Alentejo Flysch Group, Portugal, were compiled from Jorge et al. (2013). Most samples plotted in the active margin field (57 samples

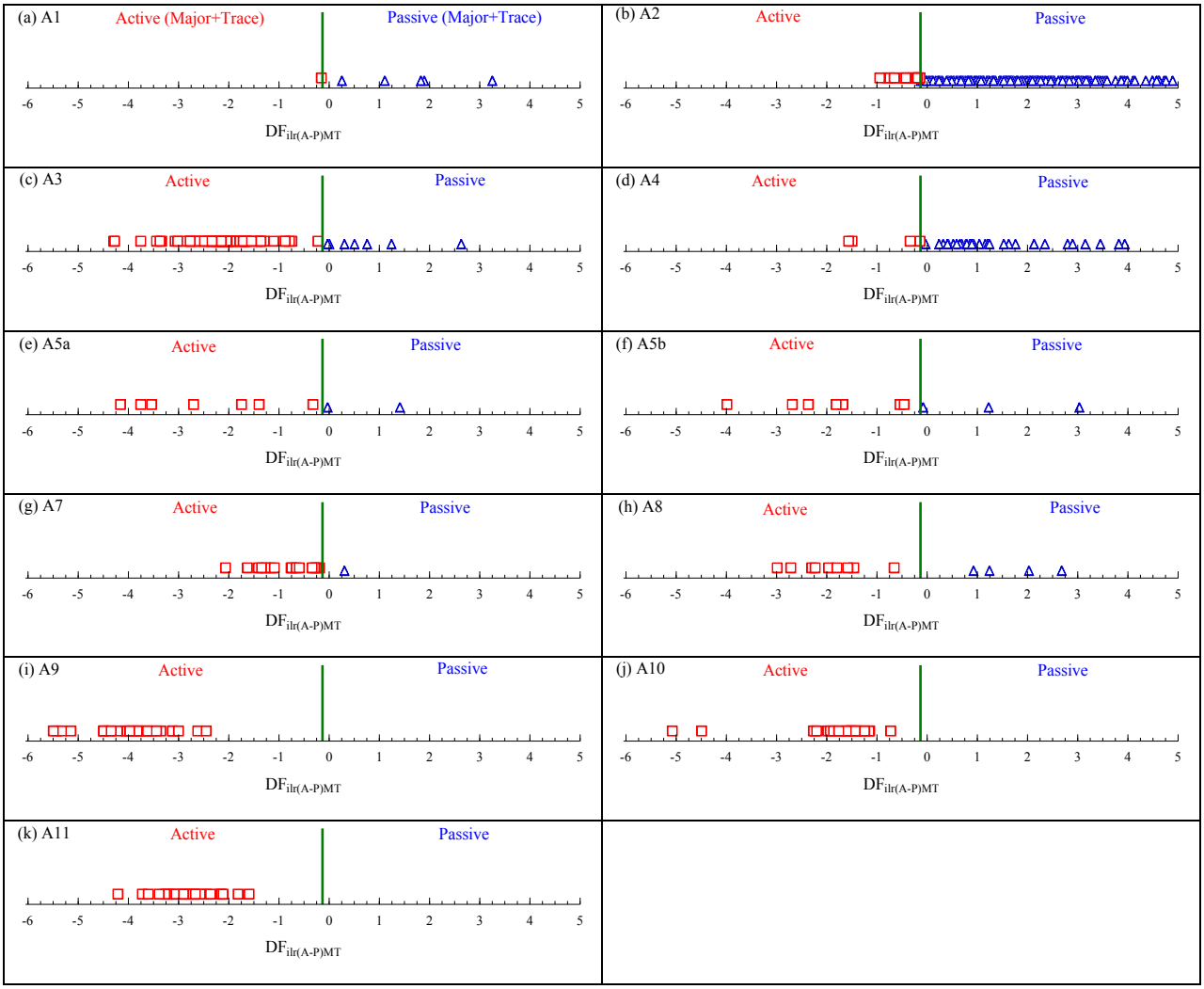

Figure 6. One-axis discriminant function $DF_{ilr(A-P)MT}$ diagram for the subdivision of Active (A) and Passive (P) margins (Table AI-12), based on isometric (i) log-ratio transformation of combined major and trace elements (MT), shows applications A1–A11 (Table 3), where a) A1: Abre et al. (2011); b) A2: Zhang et al. (2014); c) A3: Jorge et al. (2013); d) A4: Lopez et al. (2005a, b); e) A5a: Dokuz and Tanyolu (2006) ; f) A5b: Dokuz and Tanyolu (2006); g) A7: Kundu et al. (2016); h) A8: Chen et al. (2014); i) A9: Xiang et al. (2015); j) A10: Ledneva et al. (2004); k) A11: Coombs et al. (2000).

in Figures 5c and 67 samples in Figure 6c; Table 3). The mean probability values for the active margin setting were higher than those for the passive margin setting, implying that, on average, the samples plotted well within the active margin field as compared to those in the passive margin field (Figures 5c and 6c). The original authors (Jorge et al., 2013) inferred continental arc/active margin based on the diagram proposed by Bhatia and Crook (1986). Our inference of an active margin is consistent with their proposal.

3.2.4. Application study A4 (Spain)

The geochemical data for 40 Albian sandstone and siltstone samples from the Oliete Basin, Spain, were compiled from López et al. (2005a, 2005b). These samples clearly indicated a passive margin setting in both diagrams, because in Figures 5d and 6d, 39 and 36 samples, respectively were plotted in passive margin field (Table 3). The respective percent success values for the passive margin (P) were 98% and 90%, respectively, for the M and MT functions (Table 3). This interpretation is consistent with the original authors (López et al., 2005a, 2005b), who mentioned that the Iberian Plate was subjected to several periods of rifting.

3.2.5. Application study A5 (eastern Pontides, NE Turkey)

Dokuz and Tanyolu (2006) reported geochemical data for lower Jurassic (application A5a) and upper Cretaceous

(application A5b) clastic rocks from the eastern Pontides, NE Turkey, which were evaluated separately from APMdisc. The lower Jurassic rocks showed an active margin setting, because 13 out of 15 samples plotted in the major element-based diagram (Figure 5e) and 7 out of 9 in the major and trace element-based diagram (Figure 6e). The respective mean probabilities were 0.919 and 0.936 (Table 3). Similarly, the upper Cretaceous rocks from the eastern Pontides also indicated an active margin setting because 18 out of 21 plotted in the major element-based diagram (Figure 5f), with mean probability of 0.916, and 7 out of 10 in the major and trace element-based diagram (Figure 6f), with mean probability of 0.912 (86% and 70% success; Table 3). Therefore, an active margin is confirmed from both diagrams during the lower Jurassic and upper Cretaceous, which seems to be consistent with the general geology of the area. The original authors (Dokuz and Tanyolu, 2006) attempted to use the then-existing conventional ternary diagrams of Maynard et al. (1982), Roser and Korsch (1986), and Bhatia and Crook (1986), but without success. In this context, it may be noted that ternary diagrams have been shown to perform inadequately (Butler, 1979; Verma, 2015, 2020).

3.2.6. Application study A6 (Sakarya Zone, NW Turkey)

Major element geochemical data for 23 samples of Jurassic sandstone in the Sakarya Zone of NW Turkey were compiled from Sengün and Koralay (2019). Unfortunately, trace element data were not available for any of these samples. Therefore, only one diagram (Figure AII-1) could be used, which is likely to provide lower success values than the combined major and trace element-based diagram (Figure AII-2) as documented by the training set samples. Nevertheless, the major element-based diagram did not show a consistent inference, because the samples were divided in the two fields (10 in active margin with mean probability of 0.839 and 13 in passive margin with a slightly lower mean probability of 0.830; Figure 5g). However, a passive margin setting could be indicated, although the percent success of only 56% warrants caution against this inference. The original authors (Sengün and Koralay, 2019) used several different diagrams (Bhatia, 1983; Bhatia and Crook, 1986; Verma and Armstrong-Altrin, 2013) and inferred a passive margin setting, although samples were scattered in different fields and, more importantly, different indications were obtained from different diagrams (e.g., the ternary diagram of Bhatia and Crook, 1986, showed a continental island arc setting). The samples reported by Sengün and Koralay (2019) were collected from 4 different localities, although the number of samples from each area was relatively small. When these samples were processed as different sets, the samples indicated both active and passive margins (Gönen: 4 samples in active and 3 in passive; Karacabey: 1 active and 5 passive; M.kemalpaşa: 4 active and 2 passive; Bilecik: 1 active and 3 passive).

The analytical problems related to the data quality and postdepositional changes, in addition to the complex or multiple provenance of sediments, might be responsible for the conflicting indications. Furthermore, trace elements (Cr, Nb, Ni, V, Y, and Zr) should be analyzed in these samples to base the decision on the MT diagram. It is quite possible that more inferences could be obtained from the MT diagram. Some robustness inferences will be presented in a later section.

3.2.7. Application study A7 (Himalayas)

Kundu et al. (2016) reported geochemical data for Tertiary Middle Siwalik sandstones of the Himalayas. Ten and 15 samples (out of 16), with respective mean probability of 0.785 and 0.813, plotted in the active margin in Figures 5h and 6g, respectively. The expected active margin for the Himalayas, based on general geology, was thus confirmed from both diagrams (Table 2). However, from several conventional diagrams (Maynard et al., 1982; Bhatia and Crook, 1986; Kroonenberg, 1994; Cullers, 1995), the original authors inferred a passive margin setting as source rocks for their samples.

3.2.8. Application study A8 (Russia and Mongolia)

Chen et al. (2014) reported geochemical data of 15 Ordovician-Cambrian metasandstones from the Altai-Mongolian Terrane. In Figure 5i, all 15 samples plotted in the active margin field, with mean probability of 0.913 (Table 3). Among 15 samples, 9 were with complete major and trace element data, which also plotted in the active margin field (Figure 6h; mean probability of 0.965 in Table 3). Based on the tectonic discrimination diagrams of Roser and Korsch (1986) and Bhatia and Crook (1986), the original authors (Chen et al., 2014) inferred an arc setting for the sandstone samples, which is consistent with the results obtained from the discriminant functions of this study (an active margin setting).

3.2.9. Application study A9 (China)

Xiang et al. (2015) reported major and trace element data of 27 Neoproterozoic sandstone and siltstone samples from the Yangtze Block, China. All 27 samples were plotted in the active margin field in both diagrams with very high mean probability values of 0.959 and 1.000, respectively (Figures 5j and 6i; Table 3). Thus, an active margin setting can be inferred for this area during the Neoproterozoic, which is also consistent with the arc setting assigned by the original authors (Xiang et al., 2015), based on the bivariate diagrams of Roser and Korsch (1986), Bhatia and Crook (1986), and Floyd and Leveridge (1987).

3.2.10. Application study A10 (Kamchatka)

Major and trace element data for the Middle Eocene to Early Miocene shale samples from Karaginski Island,

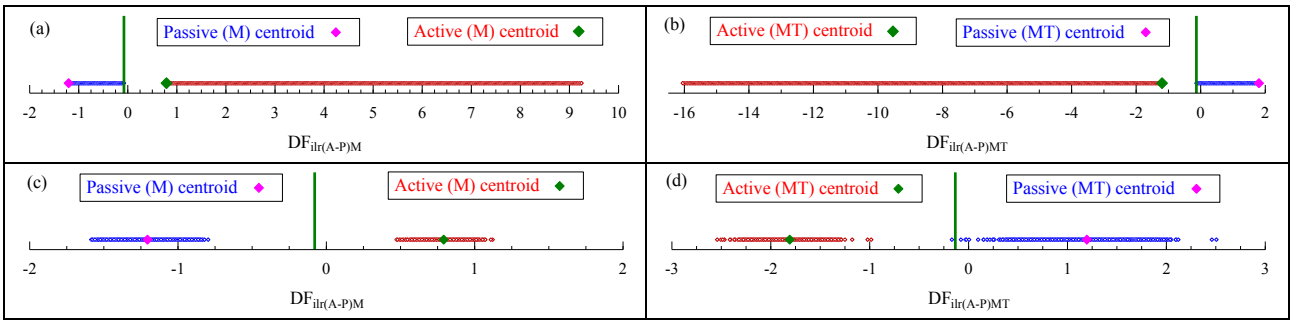

Figure 7. One-axis discriminant function diagrams for the subdivision of Active (A) and Passive (P) margins for the respective centroids and their stability against field changes and laboratory analytical uncertainties; the field change steps were (SiO_2 +0.6%; TiO_2 and P_2O_5 –0.02%; Al_2O_3 and $Fe_2O_3^t$ +0.02%; MnO +0.05%; MgO +0.8%; CaO –0.3%; Na_2O +0.4%, and K_2O –0.2%; for trace elements see the respective template at http://tlaloc.ier.unam.mx): a) active and passive centroids under the gain and loss steps in the major element-based diagram simulating field changes; b) active and passive centroids under the gain and loss steps in the major and trace element-based diagram simulating field changes; c) active and passive centroids and their 99% uncertainties in the major element-based diagram simulating laboratory changes; and d) active and passive centroids and their 99% uncertainties in the major and trace element-based diagram simulating laboratory changes.

Kamchatka, were compiled (Ledneva et al., 2004). All 25 samples were plotted in the active margin field (Figures 5k and 6j; with relatively high mean probability values of 0.887 and 0.966, respectively; Table 2). In fact, based on the trace element concentrations, the original authors (Ledneva et al., 2004) also inferred an active continental margin for the Karaginski Island shale samples.

3.2.11. Application study A11 (New Zealand)

The final application study is concerned with the Beach-Brighton Block, New Zealand, for which major and trace element data on Triassic sandstones and siltstones were compiled from Coombs et al. (2000). All samples were plotted in an active margin field in both diagrams (Figures 5l and 6k). The mean probability values were also high for the active margin (0.892 and 0.996, respectively; Table 3), indicating that the samples plotted far away from the field boundary in both diagrams. Coombs et al. (2000) also suggested an arc setting inferred from the Roser and Korsch (1986) diagram.

4. Robustness against field changes and analytical uncertainties

We illustrate the usefulness of the robustness module for testing the stability of the inference from the multidimensional discrimination of active and passive margins against field changes and laboratory uncertainties. The effect of field changes was evaluated from the percent gain and loss of elements following Verma and Díaz-González (2020). On the other hand, using the computer program UDASys3 (Rosales-Rivera et al., 2019), we calculated the centroid as well as the related 99% uncertainty of the training set samples for each margin and diagram and used them for robustness tests. These values were used for testing the robustness against analytical uncertainty. Finally, the robustness of some selected individual samples from the Sakarya Zone, NW Turkey (Sengün and Koralay, 2019), was also evaluated in terms of typical total uncertainties recently reported by Verma et al. (2018, 2019) for the analysis of geochemical reference materials.

4.1. Effect of field changes

The field changes were simulated from the compositional percent gain or loss of individual elements (in small steps) in the active and passive margin centroids, as recently done by Verma and Díaz-González (2020) for midoceanic ridge and ocean plateau centroids for postemplacement changes. We first comment on the robustness of the centroids in the major element-based diagram. The respective templates (1Template_ActiveMCentroid_field and 2TemplatePassiveMCentroid_field) for major elements are available at http://tlaloc.ier.unam.mx, in which the user can see step sizes (percent gain or loss of individual elements; see also the explanation of Figure 7a). The user can also process the templates and check the following brief description about the robustness of the centroids. Similarly, although only one set of changes was simulated, any other combination of gain or loss for all or a lesser number of elements can be evaluated.

The active margin centroid was stable (remained in the same field) for 729 steps, after which P_2O_5 concentration became too small (<0.002%) in the laboratory analysis. In the field, the maximum changes amounted to the gain or addition of +7730% SiO_2, +16% each Al_2O_3 and $Fe_2O_3^t$, +44% MnO, +33200% MgO, and +1740% Na_2O, and losses of –14% TiO_2, –89% CaO, –77% K_2O, and –14% P_2O_5. When this field-modified sample was taken to the laboratory and analyzed, the sum of all major elements would become around 100%, which is an artifact of the

closed system of compositional data (Chayes, 1971; Aitchison, 1986; Egozcue et al., 2003; Verma, 2020). In terms of compositions, these changes would amount to maximum changes as follows: +28% SiO_2, +440% MgO, and losses of all other elements (–98% to –100% TiO_2, Al_2O_3, $Fe_2O_3^t$, MnO, CaO, K_2O, and P_2O_5, and –70% Na_2O). Despite these very large changes, the active margin centroid was maintained in the same field, depicting its high robustness (Figure 7a).

The passive margin centroid was stable for 98 steps, after which it changed to the active margin. In the field, these steps amounted to gains of +80% SiO_2, +2% each Al_2O_3 and $Fe_2O_3^t$, +5% MnO, +118% MgO, and +48% Na_2O, and losses of –2% TiO_2, –26% CaO, –18% K_2O, and –2% P_2O_5. If this field-modified sample were taken to the laboratory and analyzed, the sum of all major elements would be around 100%. This amounted to maximum changes in the compositions as follows: +17% SiO_2, +42% MgO, and losses of all other elements from –32% to –36% TiO_2, Al_2O_3, $Fe_2O_3^t$, MnO, and P_2O_5 and 51% CaO, –4% Na_2O, and –46% K_2O. Despite these changes, the passive margin centroid was maintained in the same field (Figure 7a).

The MT files (3Template_ActiveMTCentroid_field and 4TemplatePassiveMTCentroid_field) are also available at http://tlaloc.ier.unam.mx, which were processed in the Robustness module. The results are shown in Figure 7b. Instead of describing in detail the relevant changes in the field and laboratory analysis, we can simply mention that similar stability of the two centroids is also demonstrated (716 and 94 steps for active and passive margins, respectively; Figure 7b).

The relatively lesser stability of the passive margin centroid as compared to the active margin is related to the combination of gain and loss of the elements evaluated (see the template files at http://tlaloc.ier.unam.mx). For other types of gains and losses of elements, the stability could be otherwise, i.e. a greater stability of the passive as compared to the active margin centroid.

4.2. Laboratory uncertainty propagation

4.2.1. Stability of active and passive margin centroids

The robustness of the centroids in both diagrams (Figure AII-1 and AII-2) was evaluated from the respective 99% uncertainties (files 1Template_ActiveMCentroid_uncertainty, 2TemplatePassiveMCentroid_uncertainty, 3Template_ActiveMTCentroid_uncertainty, and 4TemplatePassiveMTCentroid_uncertainty; all files contain rounded values according to the flexible rules put forth by Verma, 2020, and are available at http://tlaloc.ier.unam.mx). A total of 2200 replicates were generated from Monte Carlo simulations (Verma and Quiroz-Ruiz, 2006) under the model of the respective uncertainty values (Verma, 2015, 2020) and evaluated in the respective diagrams (Figure 7c for major elements and Figure 7d for major and trace elements). Both active and passive margin centroids are robust in the major element-based diagram (Figure 7c). The same is true for both centroids in the major and trace element-based diagram, except that 2 replicates (out of 2200) for the passive margin plotted in the opposite field (Figure 7d).

4.2.2. Stability of individual analysis of a sediment sample

The analytical uncertainties are seldom, if ever, presented for individual analyses, although recently Verma et al. (2018, 2019) demonstrated that it is feasible to do so provided that the calibration uncertainties are estimated and taken into account for total uncertainties. We used their total mean uncertainties to test the robustness of 4 individual samples reported by Sengün and Koralay (2019) in the Robustness module of analytical uncertainty. Only the major element-based diagram could be used. The input files (1Template_ActiveMKaracabey9_lab, 2TemplateActiveM Gönen_lab, 3Template_PassiveMKaracabey5_lab, and 4TemplatePassiveM Karacabey8B_lab) are all available at http://tlaloc.ier.unam.mx.

The active margin sample Karacabey9 close to the tectonic field boundary having a probability of about 0.6819 for this field (Figure 8a) showed that 1910 replicates (out of 2200; equivalent to 86.8%) plotted in the same field and the remaining 290 (out of 2200; equivalent to 13.2%) did so in the passive margin field. This means that there is a certain finite probability of 13.2% that a replicate analysis of sample Karacabey9 will plot in the passive margin field, although the actual composition reported by Sengün and Koralay (2019) plotted in the active margin (Figure 8a). The other active margin sample, Gönen3, with initial probability of about 0.9966, would almost always plot in its field, because out of 2200 replicates, only 1 plotted in the passive margin field (Figure 8a). Similar results were obtained for the 2 selected samples of the passive margin field (Figure 8b). Sample Karacabey5 with initial probability of 0.6330 for the passive margin field showed that about 155 replicates (out of 2200; equivalent to 7.0%) would plot in the active margin field, whereas sample Karacabey8B, with initial probability of 0.9358, would be stable in the passive margin field (Figure 8b).

The importance of estimating actual analytical uncertainty for each chemical component of a sample thus becomes clear for better understanding the inferences of multidimensional diagrams.

5. Discussion

Totally, we presented 14 test case studies and 11 application studies. Among the 14 case studies (T1–T5 and TS1–

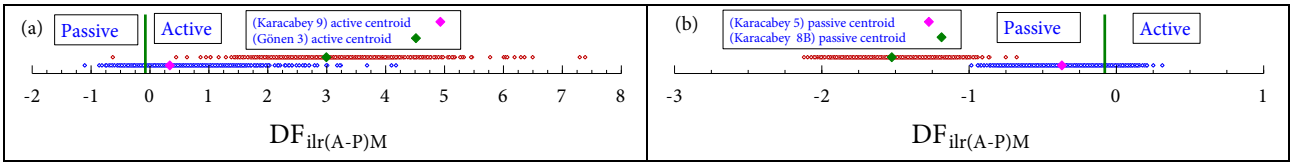

Figure 8. One-axis discriminant function diagrams for the subdivision of Active (A) and Passive (P) margins for 4 selected samples from the Sakarya Zone, NW Turkey (Sengün and Koralay, 2019) and their stability against laboratory analytical uncertainties (Verma et al., 2018, 2019) from Monte Carlo simulations: a) two active margin samples evaluated under the 99% uncertainty model; b) two passive margin samples evaluated under the 99% uncertainty model.

TS9; Tables 1 and 2), 6 represented an active margin and 8 showed a passive margin. The inferred tectonic setting based on the APMdisc program of this study is generally consistent with the conclusions derived by the original authors. It is also noted that a few authors used the discrimination diagrams of Roser and Korsch (1986), Bhatia (1983), and Bhatia and Crook (1986) to infer the tectonic setting of the study areas. Also, for 6 case studies the original authors did not discuss the tectonic setting. For these cases, we compared the results of this study with the general geology of the study areas and identified that the inferred tectonic settings are consistent with other evidence.

Similarly, the application studies (A1–A11; Table 3) indicated a passive margin for the Pavón Formation (Argentina), Scotia Basin (Canada), Oleti Basin (Spain), and Sakarya Zone (Turkey) and an active margin for the Baixo Alentejo Flysch Group (Portugal), eastern Pontides (Turkey), Middle Siwalik (Himalayas), Altai-Mongolian Terrane (Russia-Mongolia), Yangtze Block (China), Karaginski Island (Kamchatka), and Beach-Brighton Block (New Zealand). The results are generally consistent with the original authors as well as with the general geology of the study areas. The newly developed robustness module showed high robustness of field centroids against field changes and laboratory uncertainties. The effect of total uncertainty in the compositional data analysis and related multidimensional inferences was also well documented and showed that caution is required with samples plotting close to the tectonic field boundaries. Hence, based on the results obtained for the case and application studies and robustness examples, we confirm the correct functioning of the APMdisc program for the tectonic discrimination of Neoproterozoic to Holocene siliciclastic sediments/rocks.

6. Conclusions

A new online program, APMdisc, is presented to efficiently discriminate siliciclastic sediments from active and passive margin settings through the application of two multidimensional discrimination diagrams. In most test case studies, the results were satisfactory, because the expected tectonic setting was indicated by respective diagrams. For both schemes, based on major element (M) and combined major and trace elements (MT), the total probability values for the correct tectonic setting showed high average probability values in the range between 0.777 and 0.993. The application studies also showed high percent success (between 69% and 100%), except one case with low success of 56%, for the inferred tectonic margins. The new APMdisc program is available to all potential users for free, which can be used online at our web portal, http://tlaloc.ier.unam.mx.

We can conclude that independently of the type of transformation used, implementation of the multivariate technique of linear discriminant analysis (LDA) provides the same results of individual probabilities, sample counts, and percent success. The Robustness module would enable the users to evaluate their own samples for stability against field changes and laboratory uncertainties.

Acknowledgments

The first author is grateful to Direccíon General de Asuntos del Personal Académico (DGAPA) for the postdoctoral fellowship and to the Instituto de Ciencias del Mar y Limnología (ICML) for providing space to work. The second author appreciates the support received from Consejo Nacional de Ciencia y Tecnologia (CONACyT: No. A1-S-21287), DEGAPA-PAPIIT (No. IN106117 and IN107020), and Instituto de Ciencias del Mar y Limnología (ICML: no. 616) projects. We acknowledge Ing. Alfredo Quiroz Ruiz for maintaining our computing facility and updating our web portal at http://tlaloc.ier.unam.mx. We are grateful to the editor Abdurrahman Dokuz, the reviewer Abhijit Basu, and an anonymous reviewer for constructive comments to help us improve our presentation.

Availability of data and materials: Computer program availability

APMdisc is an online program and is available through our web portal at http://tlaloc.ier.unam.mx. It is free to all potential users after registration.

References

Abre P, Cingolani C, Zimmermann U, Cairncroos B, Chemale JF (2011). Provenance of Ordovician clastic sequences of the San Rafael Block (Central Argentina), with emphasis on the Ponón Trehué Formation. Gondwana Research 19: 275-290.

Aitchison J (1986). The Statistical Analysis of Compositional Data. London, UK: Chapman and Hall.

Armstrong-Altrin JS, Verma SP (2005). Critical evaluation of six tectonic setting discrimination diagrams using geochemical data of Neogene sediments from known tectonic settings. Sedimentary Geology 177: 115-129.

Basu A, Bickford ME, Deasy R (2016). Inferring tectonic provenance of siliciclastic rocks from their chemical compositions: a dissent. Sedimentary Geology 336: 26-35.

Bhatia MR (1983). Plate tectonics and geochemical composition of sandstones. Journal of Geology 91 (6): 611-627.

Bhatia MR, Crook AW (1986). Trace element characteristics of graywackes and tectonic setting discrimination of sedimentary basins. Contributions to Mineralogy and Petrology 92: 181-193.

Butler JC (1979). Trends in ternary petrologic variation diagrams - fact or fantasy? American Mineralogist 64: 1115-1121.

Chayes F (1971). Ratio correlation. A manual for Students of Petrology and Geochemistry Chicago, IL, USA: The University of Chicago Press.

Chen M, Sun M, Cai K, Buslov MM, Zhao G et al. (2014). Geochemical study of the Cambrian-Ordovician meta-sedimentary rocks from the northern Altai-Mongolian terrane, northwestern Central Asian Orogenic Belt: implications on the provenance and tectonic setting. Journal of Asian Earth Sciences 96: 69-83.

Coombs DS, Landis CA, Hada S, Ito M, Roser B et al. (2000). The Chrystalls Beach-Brighton block, southeast Otago, New Zealand: Petrography, geochemistry, and terrane correlation. New Zealand Journal of Geology and Geophysics 43: 355-372.

Cullers RL (2002). Implications of elemental concentrations for provenance, redox conditions, and metamorphic studies of shales and limestones near Pueblo, CO, USA. Chemical Geology 191: 305-327.

Cullers RL (1995). The controls on major and trace element evolution of shales, siltstones, and sandstones of Ordovician to Tertiary age in the Wet Mountains region, Colorado, USA. Chemical Geology 123: 107-131.

Dickinson WR, Suczek CA (1979). Plate tectonics and sandstone compositions. American Association of Petroleum Geologists Bulletin 63 (12): 2164-2182.

Dokuz A, Tanyolu E (2006). Geochemical constraints on the provenance, mineral sorting and subaerial weathering of Lower Jurassic and Upper Cretaceous clastic rocks of the eastern Pontides, Yusufeli (Artvin), NE Turkey. Turkish Journal of Earth Sciences 15: 181-209.

Egozcue JJ, Pawlowsky-Glahn V, Mateu-Figueras G, Barceló-Vidal C (2003). Isometric log ratio transformations for compositional data analysis. Mathematical Geology 35 (3): 279-300.

Floyd PA, Leveridge BE (1987). Tectonic environment of the Devonian Gramscatho basin, south Cornwall: framework mode and geochemical evidence from turbiditic sandstones. Journal of the Geological Society of London 144: 531-542.

Garzanti E, Resentini A (2016). Provenance control on chemical indices of weathering (Taiwan river sands). Sedimentary Geology 336: 81-95.

Imasuen OI, Fyfe WS, Olorunfemi BN, Asuen GO (1989). Zonal mineralogical/Geochemical characteristics of soils of Midwestern Nigeria. Journal of African Earth Sciences 8 (1): 41-49.

Ishiga H, Nakamura T, Sampei Y, Tokuoka T, Takayasu K (2000). Geochemical record of the Holocene Jomon transgression and human activity in coastal lagoon sediments of the San'in district SW Japan. Global and Planetary Change 25: 223-237.

Jorge RCGS, Fernandes P, Rodrigues B, Pereira Z, Olivera JT (2013). Geochemistry and provenance of the Carboniferous Baixo Alentejo Flysch Group, South Portuguese Zone. Sedimentary Geology 284-285: 133-148.

Kirkwood C, Everett P, Ferreira A, Lister B (2016). Stream sediment geochemistry as a tool for enhancing geological understanding: an overview of new data from south west England. Journal of Geochemical Exploration 163: 28-40.

Kroonenberg SB (1994). Effects of provenance, sorting and weathering on the geochemistry of fluvial sands from different tectonic and climatic environments. In: Proceedings of the 29th International Geological Congress, Part A, Kyoto, Japan, pp. 69-81.

Kundu A, Matin A, Eriksson PG (2016). Petrography and geochemistry of the Middle Siwalik sandstones (tertiary) in understanding the provenance of sub-Himalayan sediments in the Lish River Valley, West Bengal, India. Arabian Journal of Geosciences 9: 1-18.

Ledneva GV, Garver JI, Shapiro MN, Lederer J, Brandon MT et al. (2004). Provenance and tectonic settings of accretionary wedge sediments on northeastern Karaginski Island (Kamchatka, Russian Far East). Russian Journal of Earth Sciences 6 (2): 105-132.

Lee YI, Lim HS, Yoon HI (2004). Geochemistry of soils of King George Island, South Shetland Islands, West Antarctica: implications for pedogenesis in cold Polar Regions. Geochimica et Cosmochimica Acta 21: 4319-4333.

López JMG, Bauluz B, Fernández-Nieto C, Oliete AY (2005a). Factors controlling the trace-element distribution in fine-grained rocks: the Albian kaolinite-rich deposits of the Oliete Basin (NE Spain). Chemical Geology 214: 1-19.

López JMG, Bauluz B, Yuste A, Mayayo MJ, Fernández-Nieto C (2005b). Mineralogical and trace element composition of clay-sized fractions from Albian siliciclastic rocks (Oliete Basin, NE Spain). Clay Minerals 40: 565-580.

Maynard JB, Valloni R, Yu HS (1982). Composition of modern deep-sea sands from arc related basins. In: Legget JK (editor). Trench-Forearc Geology: Sedimentation and Tectonics on Modern and Ancient Active Plate Margins. London, UK: Geological Society of London Special Publications, pp. 551-561.

Ngueutchoua G, Eyong JT, Besa AZE, Agheenwi ZBA, Maschouer AE et al. (2019). Provenance and depositional history of Mesozoic sediments from the Mamfe basin and Douala sub-basin (SW Cameroon) unraveled by geochemical analysis. Journal of African Earth Sciences 158: 103550.

Papadopoulos A (2018). Geochemistry and REE content of beach sands along the Atticocycladic coastal zone, Greece. Geoscience Journal 22: 955-973.

Paul SK (2001). Geochemistry of bottom sediments from a river-estuary-shelf mixing zone on the tropical southwest coast India. Bulletin of the Geological Survey of Japan 52: 371-382.

Pe-Piper G, Piper DJ, Wang Y, Zhang Y, Trottier C et al. (2016). Quaternary evolution of the rivers of northeast Hainan Island, China: tracking the history of avulsion from mineralogy and geochemistry of river and delta sands. Sedimentary Geology 333: 84-99.

Prakash SR, Ramasamy S, Varghese NM (2018). Provenance of the Gondwana sediments, Palar Basin, Southern India. Arabian Journal of Geosciences 11: 163.

Ramos-Vázquez MA, Armstrong-Altrin JS, Machain-Castillo ML, Gío-Argáez FR (2018). Foraminiferal assemblages, ^{14}C ages, and compositional variations in two sediment cores in the western Gulf of Mexico. Journal of South American Earth Sciences 88: 480-496.

Rao W, Mao C, Wang Y, Su J, Balsam W et al. (2015). Geochemical constraints on the provenance of surface sediments of radial sand ridges off the Jiangsu coastal zone, East China. Marine Geology 359: 35-49.

Rollinson HR (1993) Using Geochemical Data: Evaluation, Presentation, Interpretation. Essex, UK: Longman Scientific Technical.

Rosales-Rivera M, Díaz-González L, Verma SP (2019) Evaluation of nine USGS reference materials for quality control through Univariate Data Analysis System, UDASys3. Arabian Journal of Geosciences 12: 40. doi: 10.1007/s12517-018-4220-0

Roser BP, Korsch RJ (1986). Determination of tectonic setting of sandstone-mudstone suites using SiO_2 content and K_2O/Na_2O ratio. Journal of Geology 94: 635-650.

Sattarova VV, Artemova AV (2015). Geochemical and micropaleontological character of Deep-Sea sediments from the Northwestern Pacific near the Kuril–Kamchatka Trench. Deep-Sea Research II 111: 10-18.

Schneider S, Hornung J, Hinderer M, Garzanti E (2016). Petrography and geochemistry of modern river sediments in an equatorial environment (Rwenzori Mountains and Albertine rift, Uganda)—implications for weathering and provenance. Sedimentary Geology 336: 106-119.

Sengün F, Koralay OE (2019). Petrography, geochemistry, and provenance of Jurassic sandstones from the Sakarya Zone, NW Turkey. Turkish Journal of Earth Sciences 28: 603-622.

Tada R, Sato S, Irino T, Matéu H, Kennett JP (2000). Millennial-scale compositional variations in late Quaternary sediments at site 1017, southern California. In: Lyle M, Koizumi I, Richter C, Moore TC Jr (editors). Proceedings of the Ocean Drilling Program, Scientific Results, Vol. 167. Washington, DC, USA: U.S. Government Printing Office, pp. 277-296.

Tapia-Fernandez HJ, Armstrong-Altrin JS, Selvaraj K (2017). Geochemistry and U-Pb geochronology of detrital zircons in the Brujas beach sands, Campeche, Southwestern Gulf of Mexico, Mexico. Journal of South American Earth Science 76: 346-361.

Tawfik HA, Salah MK, Maejima W, Armstrong-Altrin JS, Abdel-Hameed AMT et al. (2018). Petrography and geochemistry of the Lower Miocene Moghra sandstones, Qattara Depression, north Western Desert, Egypt. Geological Journal 53: 1938-1953.

Verma SP (2015). Monte Carlo comparison of conventional ternary diagrams with new log-ratio bivariate diagrams and an example of tectonic discrimination. Geochemical Journal 49 (4): 393-412.

Verma SP (2020). Road from Geochemistry to Geochemometrics. Singapore: Springer.

Verma SP, Armstrong-Altrin JS (2013). New multi-dimensional diagrams for tectonic discrimination of siliciclastic sediments and their application to Precambrian basins. Chemical Geology 355: 117-133.

Verma SP, Armstrong-Altrin JS (2016). Geochemical discrimination of siliciclastic sediments from active and passive margin settings. Sedimentary Geology 332: 1-12.

Verma SP, Díaz-González L (2020). New discriminant-function-based multidimensional discrimination of mid-ocean ridge and oceanic plateau. Geoscience Frontiers (in press).

Verma SP, Díaz-González L, Armstrong-Altrin JS (2016a). Application of a new computer program for tectonic discrimination of Cambrian to Holocene clastic sediments. Earth Science Informatics 9 (2): 151-165.

Verma SP, Quiroz-Ruiz A (2006). Critical values for six Dixon tests for outliers in normal samples up to sizes 100, and applications in science and engineering. Revista Mexicana de Ciencias Geológicas 23: 133-161.

Verma SP, Rivera-Gómez MA, Díaz-González L, Quiroz-Ruiz A (2016b). Log-ratio transformed major element-based multidimensional classification for altered High-Mg igneous rocks. Geochemistry Geophysics Geosystems 17: 4955-4972.

Verma SP, Rosales-Rivera M, Rivera-Gómez MA, Verma SK (2019). Comparison of matrix-effect corrections for ordinary and uncertainty weighted linear regressions and determination of major element mean concentrations and total uncertainties of 62 international geochemical reference materials from wavelength-dispersive X-ray fluorescence spectrometry. Spectrochimica Acta Part B 162: 105714.

Verma SP, Verma SK, Rivera-Gómez MA, Torres-Sánchez D, Díaz-González L et al. (2018). Statistically coherent calibration of X-ray fluorescence spectrometry for major elements in rocks and minerals. Journal of Spectroscopy 2018: 5837214. doi: 10.1155/2018/5837214

Vermeesch P, Garzanti E (2015). Making geological sense of 'Big Data' in sedimentary provenance analysis. Chemical Geology 409: 20-27.

Von Eynatten H, Tolosana-Delgado R, Karius V (2012). Sediment generation in modern glacial settings: grain-size and source-rock control on sediment composition. Sedimentary Geology 280: 80-92.

Xiang Z, Yan Q, White JDL, Song B, Wang Z (2015). Geochemical constraints on the provenance and depositional setting of Neoproterozoic volcaniclastic rocks on the northern margin of the Yangtze Block, China: implications for the tectonic evolution of the northern margin of the Yangtz Block. Precambrian Research 264: 140-155.

Xie Y, Chi Y (2016). Geochemical investigation of dry-and wet-deposited dust during the same dust-storm event in Harbin, China: constraint on provenance and implications for formation of Aeolian loess. Journal of Asian Earth Sciences 120: 43-61.

Young SM, Ishiga H, Roser BP, Pitawala A (2014). Geochemistry of sediments in three sectors of Trincomalee Bay, Sri Lanka: provenance, modifying factors and present environmental status. Journal of Soils and Sediments 14: 204-217.

Zaid SM, El-Badry OA, Akarish AM, Mohamed MA (2018). Provenance, weathering, and paleoenvironment of the Upper Cretaceous Duwi black shales, Aswan Governorate, Egypt. Arabian Journal of Geosciences 11: 1-17.

Zhang Y, Pe-Piper G, Piper DJW (2014). Sediment geochemistry as a provenance indicator: Unravelling the cryptic signatures of polycyclic sources, climate change tectonism and volcanism. Sedimentology 61: 383-410.

Appendix I

Table AI-1. Adjustment of major elements used for computing the isometric log-ratio (ilr) or modified log-ratio (mlr) transformations.

Function	Equation for adjustment
Fe conversion equation:	$Fe_2O_3{}^t = Fe_2O_3 + \left[FeO \times \frac{159.6882}{(2 \times 71.8444)}\right]$
SiO_2A	$\frac{100 \times SiO_2}{\left[SiO_2 + TiO_2 + Al_2O_3 + Fe_2O_3{}^t + MnO + MgO + CaO + Na_2O + K_2O + P_2O_5\right]}$
TiO_2A	$\frac{100 \times TiO_2}{\left[SiO_2 + TiO_2 + Al_2O_3 + Fe_2O_3{}^t + MnO + MgO + CaO + Na_2O + K_2O + P_2O_5\right]}$
Al_2O_3A	$\frac{100 \times Al_2O_3}{\left[SiO_2 + TiO_2 + Al_2O_3 + Fe_2O_3{}^t + MnO + MgO + CaO + Na_2O + K_2O + P_2O_5\right]}$
$Fe_2O_3{}^tA$	$\frac{100 \times Fe_2O_3{}^t}{\left[SiO_2 + TiO_2 + Al_2O_3 + Fe_2O_3{}^t + MnO + MgO + CaO + Na_2O + K_2O + P_2O_5\right]}$
MnOA	$\frac{100 \times MnO}{\left[SiO_2 + TiO_2 + Al_2O_3 + Fe_2O_3{}^t + MnO + MgO + CaO + Na_2O + K_2O + P_2O_5\right]}$
MgOA	$\frac{100 \times MgO}{\left[SiO_2 + TiO_2 + Al_2O_3 + Fe_2O_3{}^t + MnO + MgO + CaO + Na_2O + K_2O + P_2O_5\right]}$
CaOA	$\frac{100 \times CaO}{[SiO_2 + TiO_2 + Al_2O_3 + Fe_2O_3t + MnO + MgO + CaO + Na_2O + K_2O + P_2O_5]}$
Na_2OA	$\frac{100 \times Na_2O}{\left[SiO_2 + TiO_2 + Al_2O_3 + Fe_2O_3{}^t + MnO + MgO + CaO + Na_2O + K_2O + P_2O_5\right]}$
K_2OA	$\frac{100 \times K_2O}{\left[SiO_2 + TiO_2 + Al_2O_3 + Fe_2O_3{}^t + MnO + MgO + CaO + Na_2O + K_2O + P_2O_5\right]}$
P_2O_5A	$\frac{100 \times P_2O_5}{\left[SiO_2 + TiO_2 + Al_2O_3 + Fe_2O_3{}^t + MnO + MgO + CaO + Na_2O + K_2O + P_2O_5\right]}$

Table AI-2. Isometric log-ratio (ilr) transformation equations for major elements (the function ln represents natural logarithm; the final letter A after chemical symbols refers to the adjusted concentrations on an anhydrous basis to 100% with total Fe as $Fe_2O_3{}^t$; see Table AI-1 for the adjustment equations).

Isometric log-ratio	Equation for transformation
$ilr1_{TiM}$	$\sqrt{\frac{1}{2}} \times ln\{SiO_2A/TiO_2A\}$
$ilr2_{AlM}$	$\sqrt{\frac{2}{3}} \times ln\{\left[\sqrt[2]{(SiO_2A \times TiO_2A)}\right]/Al_2O_3A\}$
$ilr3_{FeM}$	$\sqrt{\frac{3}{4}} \times ln\{\left[\sqrt[3]{(SiO_2A \times TiO_2A \times Al_2O_3A)}\right]/Fe_2O_3{}^tA\}$
$ilr4_{MnM}$	$\sqrt{\frac{4}{5}} \times ln\{\left[\sqrt[4]{(SiO_2A \times TiO_2A \times Al_2O_3A \times Fe_2O_3{}^tA)}\right]/MnOA\}$
$ilr5_{MgM}$	$\sqrt{\frac{5}{6}} \times ln\{\left[\sqrt[5]{(SiO_2A \times TiO_2A \times Al_2O_3A \times Fe_2O_3{}^t \times MnOA)}\right]/MgOA\}$
$ilr6_{CaM}$	$\sqrt{\frac{6}{7}} \times ln\{\left[\sqrt[6]{(SiO_2A \times TiO_2A \times Al_2O_3A \times Fe_2O_3{}^t \times MnOA \times MgOA)}\right]/CaOA\}$
$ilr7_{NaM}$	$\sqrt{\frac{7}{8}} \times ln\{\left[\sqrt[7]{(SiO_2A \times TiO_2A \times Al_2O_3A \times Fe_2O_3{}^tA \times MnOA \times MgOA \times CaOA)}\right]/Na_2O\}$
$ilr8_{KM}$	$\sqrt{\frac{8}{9}} \times ln\{\left[\sqrt[8]{(SiO_2A \times TiO_2A \times Al_2O_3A \times Fe_2O_3{}^tA \times MnOA \times MgOA \times CaOA \times Na_2OA)}\right]/K_2OA\}$
$ilr9_{PM}$	$\sqrt{\frac{9}{10}} \times ln\{\left[\sqrt[9]{(SiO_2A \times TiO_2A \times Al_2O_3A \times Fe_2O_3{}^tA \times MnOA \times MgOA \times CaOA \times Na_2OA \times K_2OA)}\right]/P_2O_5A\}$

Table AI-3. Modified log-ratio (mlr) transformation equations for major elements (the function ln represents natural logarithm; the final letter A after chemical symbols refers to the adjusted concentrations on an anhydrous basis to 100% with total Fe as $Fe_2O_3{}^t$).

Modified log-ratio	Equation for transformation
$mlr1_{TiM}$	$\sqrt{\frac{1}{2}} \times ln\{\left[\sqrt[10]{(SiO_2A \times TiO_2A \times Al_2O_3A \times Fe_2O_3{}^tA \times MnOA \times MgOA \times CaOA \times Na_2OA \times K_2OA \times P_2O_5A)}\right] / TiO_2A\}$
$mlr2_{AlM}$	$\sqrt{\frac{2}{3}} \times ln\{\left[\sqrt[10]{(SiO_2A \times TiO_2A \times Al_2O_3A \times Fe_2O_3{}^tA \times MnOA \times MgOA \times CaOA \times Na_2OA \times K_2OA \times P_2O_5A)}\right] / Al_2O_3A\}$
$mlr3_{FeM}$	$\sqrt{\frac{3}{4}} \times ln\{\left[\sqrt[10]{(SiO_2A \times TiO_2A \times Al_2O_3A \times Fe_2O_3{}^tA \times MnOA \times MgOA \times CaOA \times Na_2OA \times K_2OA \times P_2O_5A)}\right] / Fe_2O_3{}^tA\}$
$mlr4_{MnM}$	$\sqrt{\frac{4}{5}} \times ln\{\left[\sqrt[10]{(SiO_2A \times TiO_2A \times Al_2O_3A \times Fe_2O_3{}^tA \times MnOA \times MgOA \times CaOA \times Na_2OA \times K_2OA \times P_2O_5A)}\right] / MnOA\}$
$mlr5_{MgM}$	$\sqrt{\frac{5}{6}} \times ln\{\left[\sqrt[10]{(SiO_2A \times TiO_2A \times Al_2O_3A \times Fe_2O_3{}^tA \times MnOA \times MgOA \times CaOA \times Na_2OA \times K_2OA \times P_2O_5A)}\right] / MgOA\}$
$mlr6_{CaM}$	$\sqrt{\frac{6}{7}} \times ln\{\left[\sqrt[10]{(SiO_2A \times TiO_2A \times Al_2O_3A \times Fe_2O_3{}^tA \times MnOA \times MgOA \times CaOA \times Na_2OA \times K_2OA \times P_2O_5A)}\right] / CaOA\}$
$mlr7_{NaM}$	$\sqrt{\frac{7}{8}} \times ln\{\left[\sqrt[10]{(SiO_2A \times TiO_2A \times Al_2O_3A \times Fe_2O_3{}^tA \times MnOA \times MgOA \times CaOA \times Na_2OA \times K_2OA \times P_2O_5A)}\right] / Na_2OA\}$
$mlr8_{KM}$	$\sqrt{\frac{8}{9}} \times ln\{\left[\sqrt[10]{(SiO_2A \times TiO_2A \times Al_2O_3A \times Fe_2O_3{}^tA \times MnOA \times MgOA \times CaOA \times Na_2OA \times K_2OA \times P_2O_5A)}\right] / K_2OA\}$
$mlr9_{PM}$	$\sqrt{\frac{9}{10}} \times ln\{\left[\sqrt[10]{(SiO_2A \times TiO_2A \times Al_2O_3A \times Fe_2O_3{}^tA \times MnOA \times MgOA \times CaOA \times Na_2OA \times K_2OA \times P_2O_5A)}\right] / P_2O_5A\}$

Table AI-4. Adjustment of major and trace elements used for computing the isometric log-ratio (ilr) or modified log-ratio (mlr) transformations.

Function	Equation for adjustment
Fe conversion equation	$Fe_2O_3{}^t = Fe_2O_3 + \left[FeO \times \frac{159.6882}{(2 \times 71.8444)}\right]$
SiO_2A_{MT}	$\frac{100 \times SiO_2}{\left[SiO_2 + TiO_2 + Al_2O_3 + Fe_2O_3{}^t + MnO + MgO + CaO + Na_2O + K_2O + P_2O_5 + \frac{Cr + Nb + Ni + V + Y + Zr}{10000}\right.}$
TiO_2A_{MT}	$\frac{100 \times TiO_2}{\left[SiO_2 + TiO_2 + Al_2O_3 + Fe_2O_3{}^t + MnO + MgO + CaO + Na_2O + K_2O + P_2O_5 + \frac{Cr + Nb + Ni + V + Y + Zr}{10000}\right.}$
$Al_2O_3A_{MT}$	$\frac{100 \times Al_2O_3}{\left[SiO_2 + TiO_2 + Al_2O_3 + Fe_2O_3{}^t + MnO + MgO + CaO + Na_2O + K_2O + P_2O_5 + \frac{Cr + Nb + Ni + V + Y + Zr}{10000}\right.}$
$Fe_2O_3{}^tA_{MT}$	$\frac{100 \times Fe_2O_3{}^t}{\left[SiO_2 + TiO_2 + Al_2O_3 + Fe_2O_3{}^t + MnO + MgO + CaO + Na_2O + K_2O + P_2O_5 + \frac{Cr + Nb + Ni + V + Y + Zr}{10000}\right.}$
$MnOA_{MT}$	$\frac{100 \times MnO}{\left[SiO_2 + TiO_2 + Al_2O_3 + Fe_2O_3{}^t + MnO + MgO + CaO + Na_2O + K_2O + P_2O_5 + \frac{Cr + Nb + Ni + V + Y + Zr}{10000}\right.}$
$MgOA_{MT}$	$\frac{100 \times MgO}{\left[SiO_2 + TiO_2 + Al_2O_3 + Fe_2O_3{}^t + MnO + MgO + CaO + Na_2O + K_2O + P_2O_5 + \frac{Cr + Nb + Ni + V + Y + Zr}{10000}\right.}$
$CaOA_{MT}$	$\frac{100 \times CaO}{\left[SiO_2 + TiO_2 + Al_2O_3 + Fe_2O_3{}^t + MnO + MgO + CaO + Na_2O + K_2O + P_2O_5 + \frac{Cr + Nb + Ni + V + Y + Zr}{10000}\right.}$
Na_2OA_{MT}	$\frac{100 \times Na_2O}{\left[SiO_2 + TiO_2 + Al_2O_3 + Fe_2O_3{}^t + MnO + MgO + CaO + Na_2O + K_2O + P_2O_5 + \frac{Cr + Nb + Ni + V + Y + Zr}{10000}\right.}$
K_2OA_{MT}	$\frac{100 \times K_2O}{SiO_2 + TiO_2 + Al_2O_3 + Fe_2O_3{}^t + MnO + MgO + CaO + Na_2O + K_2O + P_2O_5 + \frac{Cr + Nb + Ni + V + Y + Zr}{10000}}$
$P_2O_5A_{MT}$	$\frac{100 \times P_2O_5}{\left[SiO_2 + TiO_2 + Al_2O_3 + Fe_2O_3{}^t + MnO + MgO + CaO + Na_2O + K_2O + P_2O_5 + \frac{Cr + Nb + Ni + V + Y + Zr}{10000}\right.}$
CrA_{MT}	$\frac{100 \times Cr/10000}{\left[SiO_2 + TiO_2 + Al_2O_3 + Fe_2O_3{}^t + MnO + MgO + CaO + Na_2O + K_2O + P_2O_5 + \frac{Cr + Nb + Ni + V + Y + Zr}{10000}\right.}$
NbA_{MT}	$\frac{100 \times Nb/10000}{\left[SiO_2 + TiO_2 + Al_2O_3 + Fe_2O_3{}^t + MnO + MgO + CaO + Na_2O + K_2O + P_2O_5 + \frac{Cr + Nb + Ni + V + Y + Zr}{10000}\right.}$

Table AI-4. (Continued).

NiA_{MT}	$\frac{100 \times Ni/10000}{\left[SiO_2 + TiO_2 + Al_2O_3 + Fe_2O_3{}^t + MnO + MgO + CaO + Na_2O + K_2O + P_2O_5 + \frac{Cr + Nb + Ni + V + Y + Zr}{10000}\right.}$
VA_{MT}	$\frac{100 \times V/10000}{\left[SiO_2 + TiO_2 + Al_2O_3 + Fe_2O_3{}^t + MnO + MgO + CaO + Na_2O + K_2O + P_2O_5 + \frac{Cr + Nb + Ni + V + Y + Zr}{10000}\right.}$
YA_{MT}	$\frac{100 \times Y/10000}{\left[SiO_2 + TiO_2 + Al_2O_3 + Fe_2O_3{}^t + MnO + MgO + CaO + Na_2O + K_2O + P_2O_5 + \frac{Cr + Nb + Ni + V + Y + Zr}{10000}\right.}$
ZrA_{MT}	$\frac{100 \times Zr/10000}{\left[SiO_2 + TiO_2 + Al_2O_3 + Fe_2O_3{}^t + MnO + MgO + CaO + Na_2O + K_2O + P_2O_5 + \frac{Cr + Nb + Ni + V + Y + Zr}{10000}\right.}$

Table AI-5. Isometric log-ratio (ilr) transformation equations for major and trace elements (the function ln represents natural logarithm; the final letter A after chemical symbols refers to the adjusted concentrations on an anhydrous basis to 100% with total Fe as $Fe_2O_3{}^t$; see Table AI-4 for the adjustment equations).

Isometric log-ratio	Equation for transformation
$ilr1_{TiMT}$	$\sqrt{\frac{1}{2}} \times ln\{SiO_2A/TiO_2A\}$
$ilr2_{AlMT}$	$\sqrt{\frac{2}{3}} \times ln\{\left[\sqrt[2]{(SiO_2A \times TiO_2A)}\right]/Al_2O_3A\}$
$ilr3_{FeMT}$	$\sqrt{\frac{3}{4}} \times ln\{\left[\sqrt[3]{(SiO_2A \times TiO_2A \times Al_2O_3A)}\right]/Fe_2O_3{}^tA\}$
$ilr4_{MnMT}$	$\sqrt{\frac{4}{5}} \times ln\{\left[\sqrt[4]{(SiO_2A \times TiO_2A \times Al_2O_3A \times Fe_2O_3{}^tA)}\right]/MnOA\}$
$ilr5_{MgMT}$	$\sqrt{\frac{5}{6}} \times ln\{\left[\sqrt[5]{(SiO_2A \times TiO_2A \times Al_2O_3A \times Fe_2O_3{}^t \times MnOA)}\right]/MgOA\}$
$ilr6_{CaMT}$	$\sqrt{\frac{6}{7}} \times ln\{\left[\sqrt[6]{(SiO_2A \times TiO_2A \times Al_2O_3A \times Fe_2O_3{}^t \times MnOA \times MgOA)}\right]/CaOA\}$
$ilr7_{NaMT}$	$\sqrt{\frac{7}{8}} \times ln\{\left[\sqrt[7]{(SiO_2A \times TiO_2A \times Al_2O_3A \times Fe_2O_3{}^tA \times MnOA \times MgOA \times CaOA)}\right]/Na_2O\}$
$ilr8_{KMT}$	$\sqrt{\frac{8}{9}} \times ln\{\left[\sqrt[8]{(SiO_2A \times TiO_2A \times Al_2O_3A \times Fe_2O_3{}^tA \times MnOA \times MgOA \times CaOA \times Na_2OA)}\right]/K_2OA\}$
$ilr9_{PMT}$	$\sqrt{\frac{9}{10}} \times ln\{\left[\sqrt[9]{(SiO_2A \times TiO_2A \times Al_2O_3A \times Fe_2O_3{}^tA \times MnOA \times MgOA \times CaOA \times Na_2OA \times K_2OA)}\right]/P_2O_5A\}$
$ilr10_{CrMT}$	$\sqrt{\frac{10}{11}} \times ln\{\left[\sqrt[10]{(SiO_2A \times TiO_2A \times Al_2O_3A \times Fe_2O_3{}^tA \times MnOA \times MgOA \times CaOA \times Na_2OA \times K_2OA \times P_2O_5A)}\right]/CrA\}$
$ilr11_{NbMT}$	$\sqrt{\frac{11}{12}} \times ln\{\left[\sqrt[11]{(SiO_2A \times TiO_2A \times Al_2O_3A \times Fe_2O_3{}^tA \times MnOA \times MgOA \times CaOA \times Na_2OA \times K_2OA \times P_2O_5A \times CrA)}\right]/NbA\}$
$ilr12_{NiMT}$	$\sqrt{\frac{12}{13}} \times ln\{\left[\sqrt[12]{(SiO_2A \times TiO_2A \times Al_2O_3A \times Fe_2O_3{}^tA \times MnOA \times MgOA \times CaOA \times Na_2OA \times K_2OA \times P_2O_5A \times CrA \times NbA)}\right]/NiA\}$
$ilr13_{VMT}$	$\sqrt{\frac{13}{14}} \times ln\{\left[\sqrt[13]{(SiO_2A \times TiO_2A \times Al_2O_3A \times Fe_2O_3{}^tA \times MnOA \times MgOA \times CaOA \times Na_2OA \times K_2OA \times P_2O_5A \times CrA \times NbA \times NiA)}\right]/VA\}$
$ilr14_{YMT}$	$\sqrt{\frac{14}{15}} \times ln\{\left[\sqrt[14]{(SiO_2A \times TiO_2A \times Al_2O_3A \times Fe_2O_3{}^tA \times MnOA \times MgOA \times CaOA \times Na_2OA \times K_2OA \times P_2O_5A \times CrA \times NbA \times NiA \times VA)}\right]/YA\}$
$ilr15_{ZrMT}$	$\sqrt{\frac{15}{16}} \times ln\{\left[\sqrt[15]{(SiO_2A \times TiO_2A \times Al_2O_3A \times Fe_2O_3{}^tA \times MnOA \times MgOA \times CaOA \times Na_2OA \times K_2OA \times P_2O_5A \times CrA \times NbA \times NiA \times VA \times YA)}\right]/ZrA\}$

Table AI-6. Modified log-ratio (mlr) transformation equations for major and trace elements (the function ln represents natural logarithm; the final letter A after chemical symbols refers to the adjusted concentrations on an anhydrous basis to 100% with total Fe as $Fe_2O_3{}^t$; see Table AI-4 for the adjustment equations).

Isometric log-ratio	Equation for transformation
$mlr1_{TiMT}$	$\sqrt{\frac{1}{2}} \times ln\{(numerator)/TiO_2A\}$
$mlr2_{AlMT}$	$\sqrt{\frac{2}{3}} \times ln\{(numerator)/Al_2O_3A\}$
$mlr3_{FeMT}$	$\sqrt{\frac{3}{4}} \times ln\{(numerator)/Fe_2O_3{}^tA\}$
$mlr4_{MnMT}$	$\sqrt{\frac{4}{5}} \times ln\{(numerator)/MnOA\}$
$mlr5_{MgMT}$	$\sqrt{\frac{5}{6}} \times ln\{(numerator)/MgOA\}$
$mlr6_{CaMT}$	$\sqrt{\frac{6}{7}} \times ln\{(numerator)/CaOA\}$
$mlr7_{NaMT}$	$\sqrt{\frac{7}{8}} \times ln\{(numerator)/Na_2O\}$
$mlr8_{KMT}$	$\sqrt{\frac{8}{9}} \times ln\{(numerator)/K_2OA\}$
$mlr9_{PMT}$	$\sqrt{\frac{9}{10}} \times ln\{(numerator)/P_2O_5A\}$
$mlr10_{CrMT}$	$\sqrt{\frac{10}{11}} \times ln\{(numerator)/CrA\}$
$mlr11_{NbMT}$	$\sqrt{\frac{11}{12}} \times ln\{(numerator)/NbA\}$
$mlr12_{NiMT}$	$\sqrt{\frac{12}{13}} \times ln\{(numerator)/NiA\}$
$mlr13_{VMT}$	$\sqrt{\frac{13}{14}} \times ln\{(numerator)/VA\}$
$Mlr14_{YMT}$	$\sqrt{\frac{14}{15}} \times ln\{(numerator)/YA\}$
$mlr15_{ZrMT}$	$\sqrt{\frac{15}{16}} \times ln\{(numerator)/ZrA\}$
	where the numerator has to be calculated from the following equation:
Numerator =	$\sqrt[15]{(SiO_2A \times TiO_2A \times Al_2O_3A \times Fe_2O_3{}^tA \times MnOA \times MgOA \times CaOA \times Na_2OA \times K_2OA \times P_2O_5A \times CrA \times NbA \times NiA \times VA \times YA \times ZrA)}$

Table AI-7. Wilk's lambda and F-tests for isometric log-ratio (ilr) transformed major element variables for the two groups (active and passive margins).

Transformed variable	Wilk's lambda	F statistic	P-value
$ilr1_{TiM}$	0.568651	168.7995	0.000000
$ilr2_{AlM}$	0.587940	284.2902	0.000000
$ilr3_{FeM}$	0.542726	13.5703	0.000234
$ilr4_{MnM}$	0.549708	55.3753	0.000000
$ilr5_{MgM}$	0.540508	0.2889	0.590941
$ilr6_{CaM}$	0.647635	641.7131	0.000000
$ilr7_{NaM}$	0.564019	141.0605	0.000000
$ilr8_{KM}$	0.591124	303.3519	0.000000
$ilr9_{PM}$	0.542604	12.8385	0.000345

Table AI-8. Wilk's lambda and F-tests for isometric log-ratio (ilr) transformed major element variables for the two groups (active and passive margins).

Transformed variable	Wilk's lambda	F statistic	P-value
$ilr1_{TiMT}$	0.411171	30.6168	0.000000
$ilr2_{AlMT}$	0.421044	50.3931	0.000000
$ilr3_{FeMT}$	0.397263	2.7578	0.097176
$ilr4_{MnMT}$	0.407843	23.9510	0.000001
$ilr5_{MgMT}$	0.420889	50.0821	0.000000
$ilr6_{CaMT}$	0.412329	32.9368	0.000000
$ilr7_{NaMT}$	0.412692	33.6637	0.000000
$ilr8_{KMT}$	0.396411	1.0502	0.305781
$ilr9_{PMT}$	0.399404	7.0457	0.008105
$ilr10_{CrMT}$	0.396021	0.2700	0.603486
$ilr11_{NbMT}$	0.460669	129.7662	0.000000
$ilr12_{NiMT}$	0.408095	24.4550	0.000001
$ilr13_{VMT}$	0.396721	1.6720	0.196367
$ilr14_{YMT}$	0.420769	49.8426	0.000000
$ilr15_{ZrMT}$	0.404406	17.0663	0.000040

Appendix II

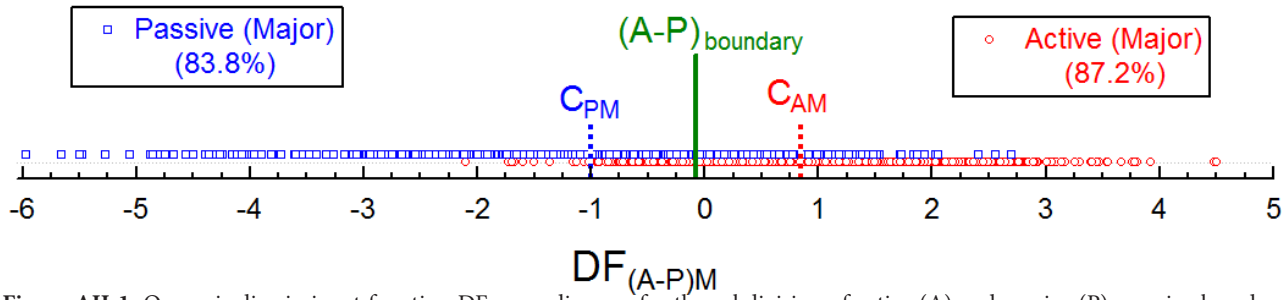

Figure AII-1. One-axis discriminant function $DF_{ilr(A-P)M}$ diagram for the subdivision of active (A) and passive (P) margins based on isometric (i) log-ratio transformation of major elements (M). The percent success values obtained for the discrimination system based on major element.

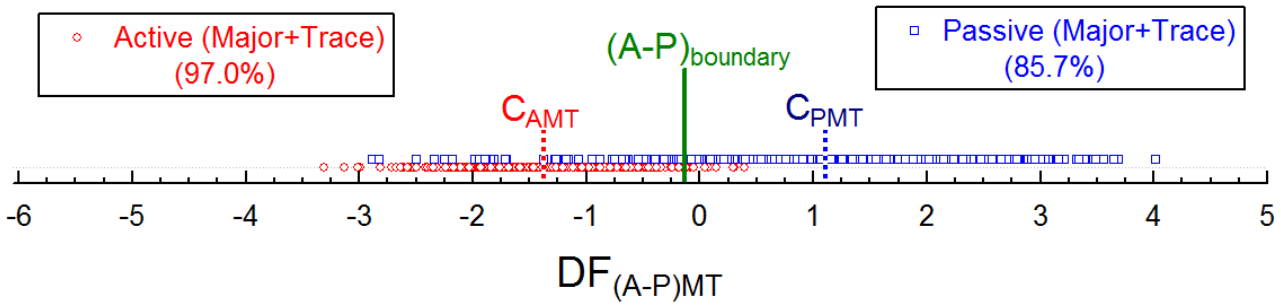

Figure AII-2. One-axis discriminant function $DF_{ilr(A-P)MT}$ diagram for the subdivision of active (A) and passive (P) margins based on isometric (i) log-ratio transformation of system based on combined major and trace elements (MT). The percent success values obtained for the discrimination system based on combined major and trace elements.

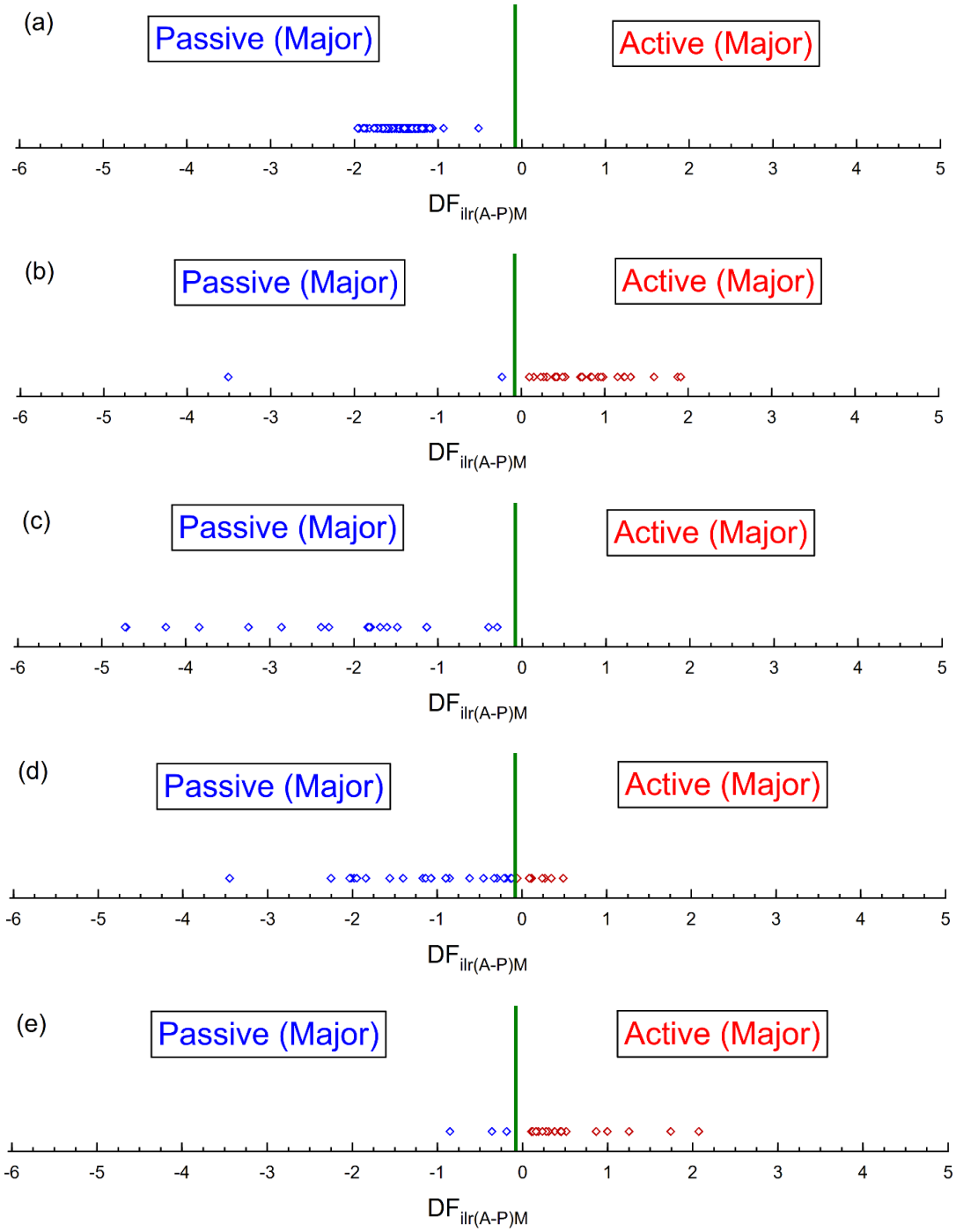

Figure AII-3. One-axis discriminant function $DF_{ilr(A\text{-}P)MT}$ diagram for the subdivision of active (A) and passive (P) margins (Table AI-8) based on isometric (i) log-ratio transformation of system based major elements (M), shows the case studies T1–T5, from a) Tada et al. (2000); b) Lee et al. (2004); c) Imasuen et al. (1989); d) Paul (2001); e) Ishiga et al. (2000).

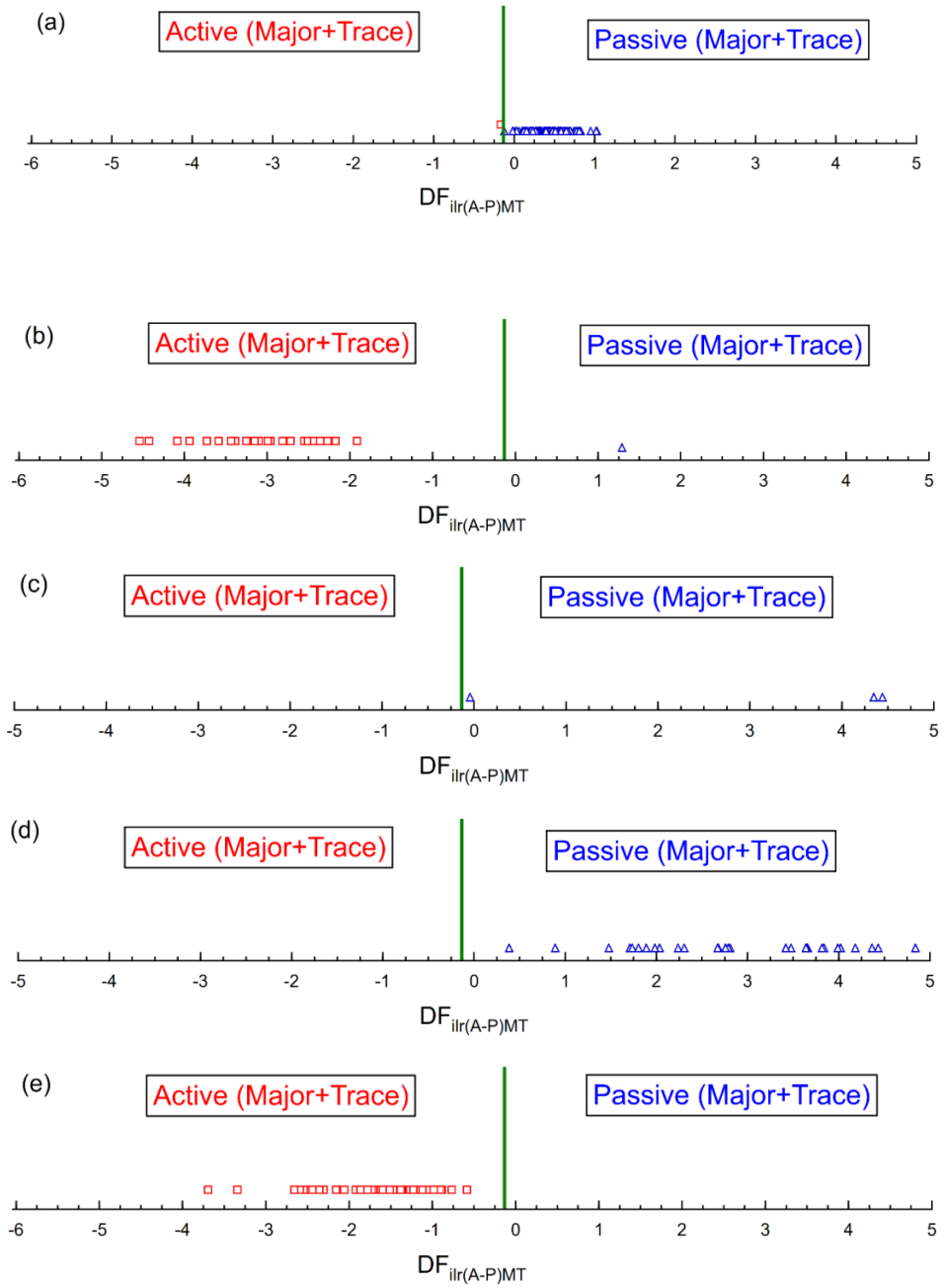

Figure AII-4. One-axis discriminant function $DF_{ilr(A\text{-}P)MT}$ diagram for the subdivision of active (A) and passive (P) margins (Table AI-8) based on isometric (i) log-ratio transformation of system based on combined major and trace elements (MT), shows case studies T1–T5, from a) Tada et al. (2000); b) Lee et al. (2004); c) Imasuen et al. (1989); d) Paul (2001); e) Ishiga et al. (2000).